Data Repository Item 2006##

Analytical methods and additional data for U-Pb geochronology, magnetic reversal stratigraphy and conodont biostratigraphy

Analytical Methods used in U-Pb Geochronology

Table DR1 presents results of high-precision uranium-lead analyses of single zircons used in the dating of volcanic ash horizons PGD-1, PGD-2, PGD-3, and GDGB-110 as discussed in the manuscript. Figure DR1 presents the concordia plots for age dates of samples PGD-1, PGD-2, PGD-3, and GDGB-110.

Zircon was separated from bulk rock samples by standard crushing, heavy liquid, and magnetic separation techniques, and was subsequently handpicked using a binocular microscope with selection based on clarity and crystal morphology. To minimize the effects of Pb-loss in our zircon, grains were pre-treated in one of two ways: removal of the outer parts of grains was accomplished by mechanical abrasion with pyrite inside air-abrasion vessels (Krogh, 1982); or, the zircon grains were treated using thermal annealing and chemical leaching (chemical abrasion or CA-TIMS technique: Mattinson, 2005) designed to preferentially remove the high-U parts of the zircon crystal that are most susceptible to Pb-loss. Annealing takes place inside a furnace at 900°C for 60 hours. The annealed grains are subsequently loaded into 200µl FEP Teflon® microcapsules and leached in 29M HF at 180°C within high-pressure Parr® vessels for 12 hours. The partially dissolved sample is then transferred into 3ml Savillex® FEP beakers, fluxed successively with 4N HNO_3 and 6N HCl over a hot plate and inside an ultrasonic bath, and thoroughly rinsed with several millilitres of ultra-pure water in between. Air-abraded zircons are cleaned in a similar fashion by fluxing in warm 4N HNO_3 in order to remove surface contaminants. After final rinsing of both air-abraded and annealed/leached zircons with ultra-pure water, zircon grains are loaded back into their microcapsules, spiked with a mixed ^{205}Pb-^{233}U-^{235}U tracer solution and dissolved completely in 29M HF at 220°C for 48-60 hours.

Dissolved Pb and U were chemically separated using a miniaturized HCl-based ion-exchange chromatography procedure modified after Krogh (1973), using 50µl columns of AG1x8 anion-exchange resin. The FEP dissolution vessels were cleaned in between analyses in four consecutive steps using concentrated HF and 6N HCl solutions at dissolution temperatures over a period of four days.

Both Pb and U were loaded with a silica gel - H_3PO_4 emitter solution (Gerstenberger and Haase, 1997) on single degassed Re filaments and their isotopic compositions were measured on the VG Sector 54 multi-collector thermal ionization mass spectrometer at MIT. Lead isotopic measurements were made in a peak-switching mode by ion counting using a Daly photomultiplier detector with a ^{206}Pb ion beam intensity of 0.5 to 2.0 x 10^{-13} amps usually maintained in the course of data acquisition. Uranium isotopes were measured as oxide ions on three Faraday detectors in a static mode with an average $^{235}U^{16}O_2^+$ ion-beam intensity of 1.0 x 10^{-12} Amps.

Measured isotopic ratios were corrected for mass-dependant isotope fractionation in the mass spectrometer, as well as for U and Pb contributions from the spike, laboratory blanks and initial Pb in the sample.

Analytical Methods used in Magnetic Reversal Stratigraphy

Figure DR2 and DR3 show the magnetostratigraphy and conodont biostratigraphy for the Upper Permian through Middle Triassic Anisian strata at Guandao section. Magnetostratigraphic data collected at Guandao defined a series of normal (10) and reverse (10) magnetozones that characterize a geomagnetic polarity record for the Lower Triassic. Detailed demagnetization experiments have resulted in the isolation of a Lower Triassic paleomagnetic directional component. Magnetostratigraphic data from Guandao was subjected to the 'reversal test' (McFadden and McElhinny, 1990) and passed at a grade 'B' level. Comparison with predicted Lower Triassic paleomagnetic directions for the Guandao locality show good agreement (derived from published paleomagnetic poles summarized by Enkin et al., 1992 and Van der Voo, 1993). Based on this evidence a primary paleomagnetic signal is interpreted.

Sampling and measurement

A total of 322 paleomagnetic samples were collected from 330 meters of steep, westerly dipping (60-70^{o}) Lower and Middle Triassic dark-grey, deep water limestone using a sampling frequency of approximately 1 meter. Cylindrical samples (diameter ~ 2.5 cm, length ~ 6-12 cm) were cored with a portable gasoline-powered drill with a water-cooled stain-less steel diamond bit. Prior to paleomagnetic samples being detached from the outcrop they were oriented using an orientation stage which determined the inclination of the core axis and a magnetic compass was used to determine the azimuth of the core axis. One sample was collected from each successive stratigraphic sampling horizon and multiple specimens prepared in the laboratory from each sample. Typically two paleomagnetic specimens were prepared from each sample with demagnetization experiments initially carried out on one of the specimens. Where magnetic polarity results were uncertain a second specimen was analyzed. Remanent magnetic measurements were made using a 2G-755R cryogenic magnetometer with a fully automated transport system and in-line 2-axis static degausser, housed in a magnetically-shielded environment at the Berkeley Geochronology Center, Berkeley, California.

The NRM of all specimens were measured and were found to range from 2.6×10^{-7} to 6.3×10^{-5} A/m. Stepwise demagnetization and measurement of magnetic remanence were performed on 452 specimens. Specimens were subjected to detailed alternating field (AF) and/or thermal demagnetization analyses. AF demagnetization was carried out on 132 specimens using a 2-axis, stationary sample, in-line demagnetizers attached to the magnetometer with 5 mT demagnetization steps up to 40 mT, followed by 10 mT increments up to 90 mT. AF demagnetization in isolation failed to remove a recent geomagnetic field overprint (Fig. DR4). Thermal demagnetization was carried out using a non-inductively wound ASC model TD48 resistance furnace (cooling chamber residual field ~2-5 nT). A total of 322 specimens were subjected to a thermal demagnetization procedure, devised according to the result of rock magnetic studies (see magnetic mineralogy section), and employing steps of 20^{o}C between 90^{o}C and 150^{o}C, 50^{o}C up to 250^{o}C and 20-25^{o}C up to 340^{o}C, and 10^{o}C up to 420^{o}C, sometimes in combination with AF demagnetization. At temperatures of 390^{o}C the NRM intensity of most samples was reduced by 98%. A 12-meter zone of the pinkish-grey limestone between 214-226 meters in the section required additional temperature steps of 25^{o}C up to 650^{o}C and 10^{o}C steps to 670^{o}C. Magnetic-susceptibility measurements using a Bartington MS-2 magnetic susceptibility

bridge were made after each thermal demagnetization step to detect mineralogical changes during heating.

Interpretable magnetostratigraphic data was obtained from 243 of the paleomagnetic samples analyzed (~54% of all specimens analyzed) enabling a paleomagnetic component of Early Triassic age to be isolated.

Magnetic mineralogy

Specimens (18) collected at regular intervals throughout Guandao section were subjected to Isothermal Remanent Magnetization (IRM) acquisition experiments and produced curves in which approximately 61% (11) of the specimens became magnetically saturated at low applied magnetic fields (0.1-0.3 T) and yielded $IRM_{0.3T}/IRM_{1.2T}$ ratio values of 0.9 or above. The remaining 7 specimens yielded $IRM_{0.3T}/IRM_{1.2T}$ ratio values of 0.8 or above (6 specimens) and <0.3 (1 specimen of pinkish grey limestone) (Fig. DR5). Preliminary magnetic mineral identification based on these experiments suggests the presence of 'magnetite' and 'hematite'.

Thermal demagnetization of a composite 3-axis IRM (Lowrie, 1990) was employed to aid further identification of the magnetic mineralogy. An IRM was applied sequentially along three orthogonal axes of the specimens using an ASC Impulse Magnetizer and decreasing magnetizing fields of 1.2T, 0.4T and 0.2T. Thermal demagnetization of the three orthogonal "soft", "medium" and "hard" IRMs , using thermal increments of 15°C to 50°C, indicated a maximum unblocking temperature of <600°C in the "hard" IRM in the vast majority of samples (94%) with a secondary unblocking temperature occurring between 320-340°C (Fig. DR6 A, B) in the "soft" and "medium" IRM. Magnetic-susceptibility measurements were made after each thermal demagnetization step to detect mineralogical changes during heating and an increase in magnetic susceptibility was observed at temperatures above 420°C in approximately 17% of specimens. Paleomagnetic thermal demagnetization experiments on typical Guandao limestone (dark-grey) showed unblocking temperatures in the range of 200°C to 550°C, commonly associated with an increase in NRM intensity and magnetic susceptibility at temperatures above 420°C.

The results of these rock magnetic studies indicate that the typical dark-grey limestone of the Guandao section are dominated by one or two low coercivity magnetic-mineral phases with unblocking temperatures of ca. 330°C ("soft" and "medium" IRM) and ca. 580°C ("hard" IRM). The lower unblocking temperature of ca. 330°C is probably indicative of an iron sulfide such as pyrrhotite, which probably formed as a result of diagenesis in the deep-water, reducing environment at the margin of the Great Bank of Guizhou where the Guandao section limestone accumulated. Further evidence that supports the 'iron sulfide' interpretation is that an increase in the magnetic moment and magnetic susceptibility during thermal demagnetization occurs at a temperature of ca. 420°C as iron sulfide oxidizes to magnetite. The higher unblocking temperature of ca. 580°C recorded by the "hard" IRM indicates the presence of either magnetite of Low Ti-titanomagnetite (Curie temperature ca. 580°C).

The presence of pyrrhotite within the Guandao section limestone provides a significant challenge to definition of a primary ChRM direction because the high stability paleomagnetic direction preserved by magnetite could only be defined between the temperature at which the pyrrhotite-bearing magnetic component is removed (320-340°C) and the temperature at which the magnetic transformation of pyrrhotite to magnetite occurs (420°C). As results stepwise thermal demagnetization experiments were devised that included multiple demagnetization steps between 320-420°C (10-20°C thermal and 5-10 mT AF demagnetization steps). This typically

resulted in higher stability paleomagnetic directions being defined by only three demagnetization vectors. The application of field tests, such as the bedding tilt and reversals test, to the demagnetization data were used to establish the primary nature of the paleomagnetic directional data defined by the thermal demagnetization experiments (see reliability of paleomagnetic data section).

Thermal demagnetization of a composite 3-axis IRM on one specimen of pinkish-grey limestone required temperature steps of 25°C up to 650°C and 10-25°C steps to 700°C for complete demagnetization to be achieved (Fig. DR6 C). The "soft", "medium" and "hard" IRMs all indicate an unblocking temperature of approximately 650-675°C. Magnetic susceptibility measurements increased at temperatures above 475°C. Paleomagnetic thermal demagnetization experiments on multiple specimens (n = 26) of pinkish-gray limestone showed consistent demagnetization behavior with unblocking temperatures in the range of 650-675°C and no increase in NRM intensity or susceptibility at higher temperatures. This suggests the presence of a high unblocking temperature magnetic-mineral phase (i.e. hematite) occurring over a 12 meter interval between 214-226 meters in the Guandao section. Demagnetization experiments of NRM over this interval were designed to incorporate multiple steps between 420°C and 680°C to adequately define the most stable magnetic component.

Characteristic remanent magnetization (ChRM) directions were identified from the demagnetization data by analyzing stereographic projections and Zijderveld diagrams ('z-plots'). ChRM directions were determined by principal component analysis (Kirschvink, 1980).

Demagnetization behavior

During demagnetization experiments a downward-directed vector was removed during the initial thermal or AF demagnetization steps in almost all samples. In most cases this downward vector is northerly and corresponds approximately to the current dipole or modern field direction (Fig. DR7 A (i), C (i) and D (i)). In other specimens, this initial downward direction is intermediate between normal and reverse dipole field directions, suggesting the initial removal of more than one magnetic component (Fig. DR7 B (i)). The initial northerly, downward magnetic component was typically removed at temperature between 250-320°C (Fig. DR7 B (iii & iv), C (iii & iv) and D (iii & iv)). A recent geomagnetic-field declination (D) and inclination (I) of approximately of 9° and 45°, respectively, were observed from the results of the AF demagnetization analyses and up to temperatures of 250-300°C (Fig. DR7).

In fifty-four percent of the samples this normal polarity direction is followed by a downward south-easterly (Fig. DR7 B (i) and C (i)) or a upward north-westerly directed vector (Fig. DR7 A (i)). These vectors were typically defined between 340-420°C. In some specimens of pinkish-grey limestone these directions persisted to beyond 600°C. Application of a structural correction resulted in the downward south-easterly directed vector assuming an upward south-easterly direction. We interpret this as indicative of a reverse polarity direction that has undergone a subsequent tectonic rotation to the west of ca. 50°. Conversely, application of a structural correction causes the upward north-westerly directed vector to assume a downward north-westerly direction. We interpret this as a normal polarity direction that has been rotated to the west by ca. 50°.

A steady decline in magnetic intensity was observed during both AF and thermal demagnetization. An unblocking temperature of ca. 110-130°C was observed in some samples (Fig. DR7 C (iv)) and is interpreted as removal of a paleomagnetic component probably carried by goethite. A more stable magnetic component unblocks at a temperature between 250-340°C

and is most likely associated with the destruction of magnetic component carried by pyrrhotite. Magnetic intensity continues to decrease and is typically reduced by 98% at temperatures of ca. 390°C. An increase in NRM intensity combined with rapidly increasing magnetic susceptibility was observed in some specimens at temperatures above 420°C. The remaining forty-six percent of thermal demagnetization experiments analyzed revealed specimens that became magnetically unstable at temperatures above 420°C as evidenced by a rapid increase in NRM intensity and magnetic susceptibility and random paleomagnetic directions.

Primary paleomagnetic directional components were obtained from 243 thermally demagnetized specimens. A mean primary paleomagnetic declination of 55° and inclination of 21° (alpha 95=10.8°, R =195.5) for the Guandao section was observed after structural correction.

Reliability of paleomagnetic data

During this study reliability criteria were adopted to provide an unbiased appraisal of the quality of the paleomagnetic data. Only stable magnetic components defined between 250°C and 700°C or between 10 mT and 90 mT on samples previously heated to a minimum of 200°C (n= 1) but typically 320 °C were used to define ChRM directions and used to define a reversal stratigraphy. Components in which over one-half the straight line segment on a z-plot was defined at a lower temperature were only used as supporting evidence for polarity definition. Directions were determined where demagnetization segments were linear, with maximum angular deviations (MAD) <20°, and defined by 3 or more consecutive demagnetization vectors. Ninety-one percent of the paleomagnetic data used to define the reversal stratigraphy of this study possessed MAD values <20°, while sixty-six percent of the data possessed MAD values <15°. Paleomagnetic directions with high unblocking temperatures (>575°C), which appear to be carried by hematite, were included because of the successful passage of a 'hematite only' reversal test (see point 3 below).

We consider the ChRM to be of primary origin for the following reasons:

1. Normal and reverse directions were detected. All ChRM reverse and normal polarity data acquired from the 243 specimens pass the reversal test (i.e. computation of mean directions, and confidence intervals about those mean directions, for both normal- and reverse-polarity groups and comparison of one mean direction with the antipode of the other direction; Fig. DR8). According to the scheme of McFadden and McElhinny (1990), the reversal test is positive (N_{rev} = 125, N_{norm} = 118, R_{rev} = 101.86, R_{norm} = 95.08, ($_b$ = 8.78°) and belongs to the R_b rank (5°≤($_b$ ≤10°). Passage of the reversal test indicates that the ChRM directions are free of secondary NRM components and that the paleomagnetic data has adequately averaged secular variation. Since the sets of normal- and reversed-polarity sampling sites conform to stratigraphic layering, the ChRM direction is probably primary.
2. The paleomagnetic directional data from the Guandao section ($D_{mean\ GD}$ = 55.3°, $I_{mean\ GD}$= 21.0°, $\forall_{95}$ = 10.8°, *R* = 195.5, *k* = 5.0, N = 243) are in general agreement with predicted Lower Triassic paleomagnetic directions for the Guandao locality ($D_{pub.\ data}$ = 35.3°, $I_{pub.\ data}$ = 23.6°, $\forall_{95}$ = 5.1°, *R* = 13.1, *k* = 14.5, N = 14) based on published Lower Triassic paleomagnetic poles for the South China Block (SCB) (summarized by Enkin et al.,1992 and Van der Voo, 1993) (Fig. DR9). Statistical comparison (*F* statistic) indicates that the Guandao site mean ($D_{mean\ GD}$ = 55.3°, $I_{mean\ GD}$ = 21.0°, $\forall_{95}$ = 10.8°) and the mean Lower Triassic SCB paleomagnetic direction for the Guandao locality derived previously published paleomagnetic poles ($D_{pub.\ data}$ = 35.3°, $I_{pub.\ data}$ = 23.6°, $\forall_{95}$ = 5.1°, *R* = 13.1, *k*

= 14.5, N = 14) are the same at a 95% confidence level (i.e. the observed *F* statistic (F_{obs} = 0.71) is less than tabulated *F* statistic ($F_{tab, 2, 26}$ = 3.37) at a significance level of 95%, and thus the two mean directions are the same at the 95% level of significance). We conclude from the outcome of these tests that the Lower Triassic ChRM direction from Guandao is the same as the predicted Lower Triassic paleomagnetic direction based on previously published paleomagnetic poles and therefore the ChRM defined in this study is primary.

3. The high stability ChRM defined at temperatures between 320-420°C and above is carried by stable magnetite (or low Ti-Titanomagnetite) (Fig. DR6 A and B). A reversal test (Fig. DR10), based on primary ChRMs defined by high unblocking temperature specimens (up to 680°C), is negative (N_{rev} = 4, N_{norm} = 21, R_{rev} = 9.06, R_{norm}= 19.95, ($_c$ = 20.27°) and with ($_c$ >20°, indicating the normal and reverse hematite ChRMs were not acquired at the same time or that secondary magnetic component has not been completely removed or that secular variation has not been adequately sampled. However, comparison of the Guandao ChRM directions recorded by hematite (D_{hem} = 33.1°, I_{hem}= 12.2°, $\forall_{95}$ = 15.8°, *R* = 23.3, *k* = 24.4, N = 25) and magnetite (or Low Ti-Titanomagnetite) (D_{mag} = 58.4°, I_{mag}= 21.5°, $\forall_{95}$ = 10.0°, *R* = 174.0, *k* = 4.9, N = 218) indicate general agreement with predicted Lower Triassic paleomagnetic directions for the Guandao locality ($D_{pub. data}$ = 35.3°, $I_{pub. data}$ = 23.6°, $\forall_{95}$ = 5.1°, *R* = 13.1, *k* = 14.5, N = 14). The observed *F* statistic for the magnetite ChRM ($F_{obs\ mag}$ = 0.93) and the hematite ChRM ($F_{obs\ hem}$ = 0.22) are less than tabulated *F* statistic ($F_{tab, 2, 26}$ = 3.37) at a significance level of 95%, and thus the mean ChRM directions preserved by magnetite and hematite are the same as the predicted direction for the Guandao locality at the 95% level of significance. We conclude from the outcome of these tests that the Lower Triassic ChRM direction from Guandao recorded by hematite and magnetite are the same as the predicted Lower Triassic paleomagnetic direction based on previously published paleomagnetic poles and therefore the ChRM defined from the higher unblocking temperature magnetic components (>320°C) is primary, though the ChRM hematite directions appear to be contaminated by a secondary magnetic component or have not adequately sampled for secular variation.
4. In the majority of samples the NRM and low stability magnetic overprint is carried by minerals with low coercivity (up to 90 mT) and low unblocking temperatures (<320-340°C). Prior to structural correction this magnetic component has a direction ($D_{recent\ bbc}$ = 8.8°, $I_{recent\ bbc}$ = 45.3°, $\forall_{95}$ = 6.2°, N = 267) that is different from the ChRM carried by more stable magnetic minerals in the same rock ($D_{mean\ GD\ bbc}$ = 52.1°, $I_{mean\ GD\ bbc}$ = -40.4°, $\forall_{95}$ = 11.9°, N = 243) but similar to the present day field geomagnetic field direction at Guandao ($D_{present\ day}$ = 9°, $I_{present\ day}$ = 44°) (Fig. DR11). We can conclude that the low stability magnetic overprint was acquired post-folding of the Guandao section and it's similarity with the present day field direction indicates that it was acquired relatively recently.
5. Structural corrections applied to the ChRM data result in an improvement in the directional sense and clustering of the ChRM defined from the Guandao section ($D_{mean\ GD\ bbc}$ = 52.1°, $I_{mean\ GD\ bbc}$ = -40.4°, $\forall_{95}$ = 11.9° to $D_{mean\ GD\ abc}$ = 55.5°, $I_{mean\ GD\ abc}$ = 21.0°, $\forall_{95}$ = 10.8°) indicating that the most stable magnetic component was acquired prior to folding. Though all the ChRM data comes from one locality the bedding tilts are sufficiently different for this result to constitute a statistically significant passage of the

bedding tilt test at a significance level 95% (i.e. for the Guandao section Limestone, N = 243, k_b = 4.17, k_a = 5.09, and k_a/k_b = 1.22. The degrees of freedom are 2(N-1) = 486, and the *F*-distribution value $F_{486,486}$ for 5% significance level is ca. 1.00. With the ratio $k_a/k_b > F_{486,486}$, the improvement in grouping produced by applying a structural correction is significant at the 5% level). Since it has been shown that the structural correction results in a significant reduction in dispersion of the site mean ChRM direction it can be concluded that the magnetostratigraphy pre-dates the time of folding (i.e. pre- Late Cretaceous (Opdyke et al., 1986).

Magnetostratigraphic results

The magnetic polarity of the ChRM, defined by incremental demagnetization studies, is plotted, together with declination, inclination, and the virtual geomagnetic polar latitudes (VGP) for the Guandao section is summarized in Figure DR2. Declination, inclination and VGP latitude are corrected for the tectonic rotations observed at the Guandao locality. This correction was achieved by calculating the difference in declination and inclination between the site-mean ChRM ($D_{mean\ GD} = 55.3^o$, $I_{mean\ GD} = 21.0^o$) and the site geomagnetic field direction as predicted by the geocentric axial dipole model ($D_{ax} = 0^o$, $I_{ax} = 43.8^o$), and rotating declination and inclination of each sample site ChRM by the calculated difference.

Magnetic polarity definition is based on VGP latitude. Southerly VGP latitudes (negative) are interpreted as reverse polarity whereas northerly VGP latitudes (positive) are interpreted as normal. In Figure DR2 magnetozone definition is based on a minimum of two consecutive specimens exhibiting the same polarity and MAD values less than 20^o (n = 220). Individual specimens that show opposite polarity to adjacent specimens are indicated by half bars in the magnetic polarity column of Figure DR2. The remaining 23 interpretable specimens (MAD > 20^o) were used to better define magnetozone boundaries. Ten normal-polarity and ten reverse-polarity magnetozones were defined during this study. Correlation of the Olenekian-Anisian magnetostratigraphy of Guandao section with the western Tethyan compilation of Muttoni et al., (2000) and global compilation of Ogg (2004) is presented in figure DR3.

Conodont Biostratigraphic Calibration to Substages of the Anisian

The substages of the Early Anisian were originally defined on the basis of ammonoid biostratigraphy (Assereto, 1974). In this paper we have used conodonts as a proxy for placement of the Olenekian-Anisian boundary and the substages of the Anisian (Fig. 2, DR3).

The basal substage of the Anisian is the Aegean, with its type area on the island of Chios, Greece, and with its basal boundary corresponding to the Olenekian-Anisian boundary defined by the first appearances of the ammonoids *Paracrochordiceras and Japonites* (Assereto, 1974). We have used *Chiosella timorensis* to define the Olenekian-Anisian boundary (Fig. 2, DR3). *Cs. timorensis* has been recognized as a key index fossil for definition of this boundary and the International Commission on Stratigraphy has informally agreed that the first appearance of *Cs. timorensis* at the Desli Caira section in Dobrogea, Romania could serve as a GSSP for the O-A boundary (Orchard, 1995; Orchard and Tozer, 1997; ICS, 2004). The second substage of the Anisian is the Bithynian, with its type area in the Kokaeli peninsula of Turkey and with its base defined by the first occurrence of the *Osmani* ammonoid zone, and containing ammonoids of the *Ismidiscus* zone (Assereto, 1974). The third substage is the Pelsonian, with its type area in the

Balaton Highland of Hungary, and with its base defined by the first appearance of the ammonoid *Balatonites balatonicus* (Assereto, 1974 and references therein).

We have used the first appearance of the conodont *Nicoraella germanica* to place the basal boundary of the Bithynian and the first appearance of the conodont *Nicoraella kockeli* to place the basal boundary of the Pelsonian in our study (Fig. 2, DR3). Within the Pelsonian both species occur (Fig. 2, DR3).

Pelsonian strata in the type area of the Balaton Highlands contain the conodonts *Ni. kockeli* and *Ni. germanica* co-occurring with *Balatonites balatonicus* (Vörös, 2003). Underlying strata assigned to the Bithynian in this area contain the conodont *Ni. germanica* but lack *Ni. kockeli* (Vörös, 2003).

Bithynian strata of the type area of the Kokaeli peninsula of Turkey contain the first appearance of *Ni. germanica* about 5 m before the base of the *Osmani* ammonoid zone and above the last occurrence of *Neogondolella regalis* (Nicora, 1977). The first occurrence of *Ni. germanica* thus closely approximates the basal Bithynian boundary as defined by ammonoids.

The conodont succession from other sections in Chios, the Germanic basin, and Sicily also support the use of *Ni. germanica and Ni. kockeli* for placement of substage boundaries. In the Germanic basin, *Ni. kockeli* co-occurs with Pelsonian ammonoids and underlying strata assigned to the Bithynian contain *Ni. germanica* but lack *Ni. kockeli* (Kozur, 1974a; 1974b; personal communication, 2006). Strata of the underlying Aegean substage, in the type area of Chios, Greece, in the Germanic Basin and Sicily, contain the conodonts *Cs. timorensis* and *Neogondolella regalis*, but lack *Ni. germanica* (Nicora, 1977; Kozur, 1974a; 1974b; 2003). This observation further supports use of the first appearance of *Ni. germanica* in the placement of the basal boundary of the Bithynian.

References

Assereto, R., 1974, Aegean and Bithynian, proposal for two new Anisian substages: Schriftenreihe der Erdwissenschaftlichen Kommissionen, Österreichische Akademie der Wissenschaften, vol. 2: page 23-39.

Chan L.S., C.Y. Wang, and X.Y. Wu, 1984, Paleomagnetic results from some Permian-Triassic rocks from southwestern China, Geophysical Research Letters, v. 96, 327-335.

Enkin, R.J., Zhenyu Yang, Yan Chen, and Courtillot, V., 1992, Paleomagnetic constraints on the geodynamic history of the major blocks of China from the Permian to the Present: Journal of Geophysical Research, v. 97, n. B10, p. 13,953-13,989.

Enkin, R.J., 1990, Formation et déformation de l'Asie depuis la fin de l'ère primaire: les apports de l'étude paléomagnétique des formations secondaires de Chine du Sud, 1990, Ph.D thesis, Univ. de Paris 7., 333 pp.

Gerstenberger, H. and Haase, G., 1987, A highly effective emitter substance for mass spectrometric Pb isotope ratio determinations: Chemical Geology: v.136, n. 3-4, p, 309-312.

Heller, F., W. Lowrie, H. Li, and J. Wang, 1988, Magnetostratigraphy of the Permo-Triassic boundary section at Shangsi (Guangyuan, Sichuan, China), Earth Planet. Sci. Lett., v. 88, 348-356.

ICS (International Commission on Stratigraphy), 2004, Consolidated Annual Report, compiled by Gradstein, F. M., and Ogg, J. G., www.stratigraphy, org.

Jaffey, A.H., Flynn, K.F., Glendenin, L.E., Bentley, W. C., and Essling, A.M., 1971, Precision measurement of half-lives and specific activities of 235U and 238U: Physical Review, v. C, no. 4, p. 189-1906.

Kirschvink, J.L., 1980, The least-squares line and plane and analysis of paleomagnetic data. Geophys. J.R. Astron. Soc., v. 62, 699-718.

Kozur, H. W., 2003, Integrated ammonoid, conodont and radiolarian zonation of the Triassic: Hellesches Jahrbuch Geowissenschaften, v. B25, p. 49-79.

Kozur, H., 1974 a, Biostratigraphie der germanischen Mitteltrias. Teil I: Freiberger Forsch.-H., Leipzig, v. C 280, p. 1-56, 12 tabs.

Kozur, H., 1974 b, Biostratigraphie der germanischen Mitteltrias. Teil II: Freiberger Forsch.-H., Leipzig, v. C 280, p.1-70,

Krogh, T. E.,1973, A low contamination method for hydrothermal decomposition of zircon and extraction of U and Pb for isotopic age determination: Geochimica et Cosmochimica Acta, v. 37, p. 485-494.

Krogh, T.E., 1982, Improved accuracy of U–Pb zircon ages by the creation of more concordant systems using an air abrasion technique: Geochimica et Cosmochimica Acta, v. 46, p. 637–649.

Li, H., and Z. Wang, 1987, Magnetostratigraphy of the Permo-Triassic boundary sections at Changxing, Zhejiang province China (in Chinese), in Abstracts for the Third National Symposium on Paleomagnetism, Geophysical Society of China, Guangzhou, People's Republic of China.

Lin, J.L., 1984, The apparent polar wander paths for the North and South China blocks, Ph.D. thesis, Univ. of Calif., Santa Barbara, 248 pp.

Lin, J.L., M. Fuller, and W. Y. Zhang, 1985, Preliminary Phanerozoic polar wander paths for the North and South China blocks: Nature, 313, v. 444-449.

Lowrie, W., 1990, Identification of ferromagnetic minerals in a rock by coercivity and unblocking temperature properties, Geophysical Research Letters, v. 17, 159-162.

Ma, X., and Z. Zhang, 1989, Paleomagnetic study of Late Permian rocks from Sichuan Emei region and Shanxi Taiyuan region (in Chinese), Acta Geophysica Sinica, v. 32, 451-465.

Mattinson, J.M., 2005, Zircon U–Pb chemical abrasion (CA-TIMS) method: Combined annealing and multi-step partial dissolution analysis for improved precision and accuracy of zircon ages: Chemical Geology, v. 220 p. 47–66.

McElhinny, M.W., B.J.J. Embleton, X. Ma, and Z. Zhang, 1981, Fragmentation of Asia in the Permian, Nature, v. 239, 212-216.

McFadden, P.L. and McElhinny, M.W., 1990, Classification of the reversal test in paleomagnetism, Geophys. J. int., v. 103, 725-729.

Muttoni, G., Gaetani, M., Budurov, K., Zagorchev, I., Trifonova, E., Ivanova, D., Petrounova, L. and Lowrie, W. 2000, Middle Triassic paleomagnetic data from northern Bulgaria; constraints on Tethyan magnetostratigraphy and paleogeography: Palaeogeography, Palaeoclimatology, Palaeoecology, v. 160, no. 3-4, p. 223-237.

Nicora, A., 1977, Lower Anisian platform conodonts from the Tethys and Nevada: Taxonomic and stratigraphic revision: Palaeontographica, v. A 157, p. 88-107.

Ogg, J. G., 2004, The Triassic Period, *in* Gradstein, F. M., Ogg, J.G., and Smith, A.G., eds., A geologic time scale 2004: Cambridge University Press, Cambridge, U.K., 589 p.

Opdyke, N.D., K. Huang, G. Xu, W. Y. Zhang, and D.V. Kent, 1986, Paleomagnetic results from the Triassic of the Yangtze Platform, Journal of Geophysical Research, v. 91, 9553-9568.

Orchard, M. J., 1995, Taxonomy and correlation of Lower Triassic (Spathian) segminate conodonts from Oman and revision of some species of Neospathodus: Journal of Paleontology, v. 69, p. 110-122.

Orchard, M. J., and Tozer, E. T., 1997, Triassic conodont biochronology, its calibration with the ammonoid standard, and a biostratigraphic summary for the western Canada sedimentary basin: Bulletin of Canadian Petroleum Geology, v. 45, p. 675-692.

Steiner, M., J. Ogg, Z. Zhang, and S. Sun, 1989, The late Permian/early Triassic magnetic polarity time scale and plate motions of South china, Journal of Geophysical Research, v. 94, 7343-7363.

Vander Voo, R., 1993, Paleomagnetism of the Atlantic, Tethys and Iapetus oceans: Cambridge University Press, Cambridge, 411 p.

Vörös, A., 2003, The Pelsonian Substage on the Balaton Highland (Middle Triassic, Hungary): Geologica Hungarica, Series Palaeontologica, v.55, 195 pp.

Zhu, Z. W., T. Hao, and H. Zhao, 1988, Paleomagnetic study on the tectonic motion of the Pan-Xi block and adjacent area during the Yin Zhi-Yanshan period (in Chinese), Acta Geophys. Sinica, 31, 420-431.

TABLE DR-1. U-Pb ZIRCON DATA FOR ASH BEDS FROM THE GUANDAO SECTION, SOUTH CHINA.

Sample Fractions (a)		Pb_c (pg) (b)	$\frac{Pb^*}{Pb_c}$ (b)	$\frac{Th}{U}$	$\frac{206\ Pb}{204\ Pb}$ (c)	$\frac{^{208}Pb}{^{206}Pb}$ (d)	Ratios $\frac{^{206}Pb}{^{238}U}$ (e)	err (2σ%)	$\frac{^{207}Pb}{^{235}U}$ (e)	err (2σ%)	$\frac{^{207}Pb}{^{206}Pb}$ (e)	err (2σ%)	Age (Ma) $\frac{^{206}Pb}{^{238}U}$	$\frac{^{207}Pb}{^{235}U}$	$\frac{^{207}Pb}{^{206}Pb}$	corr. coef.
GDGB Tuff-110																
z25	ac	0.6	513.0	0.514	28072.3	0.179	0.374300	(.07)	8.2967	(.09)	0.16076	(.06)	**2049.6**	**2264.0**	**2463.7**	0.774
z20	ac	1.5	90.6	0.216	5014.5	0.156	0.190364	(.12)	4.5485	(.16)	0.17329	(.11)	**1123.3**	**1739.9**	**2589.7**	0.744
z10	aa	0.6	21.8	0.633	1167.1	0.327	0.075398	(.18)	0.6730	(.34)	0.06474	(.27)	**468.6**	**522.5**	**765.7**	0.607
z21	ac	0.6	181.1	0.087	11936.0	0.050	0.067316	(.11)	0.5993	(.19)	0.06457	(.15)	**420.0**	**476.8**	**760.3**	0.590
z12	aa	0.5	32.5	0.452	1932.8	0.184	0.068966	(.15)	0.5582	(.33)	0.05870	(.27)	**429.9**	**450.3**	**556.0**	0.565
z11	aa	0.6	12.2	0.314	759.5	0.152	0.050664	(.27)	0.3971	(.39)	0.05684	(.27)	**318.6**	**339.5**	**485.4**	0.721
z26	ac	0.4	120.9	0.427	7387.9	0.149	0.052212	(.08)	0.3872	(.15)	0.05378	(.13)	**328.1**	**332.3**	**361.9**	0.514
z9	aa	0.8	3.9	0.330	259.2	0.129	0.049280	(.79)	0.3687	(1.86)	0.05427	(1.59)	**310.1**	**318.7**	**382.1**	0.531
z(2)	ac	0.9	42.0	0.180	2798.2	0.057	0.039142	(.10)	0.2762	(.21)	0.05118	(.18)	**247.5**	**247.6**	**248.7**	0.513
z1	aa	0.5	7.0	0.493	440.2	0.161	0.038977	(.45)	0.2756	(.80)	0.05128	(.63)	**246.5**	**247.2**	**253.7**	0.616
z2	aa	0.5	33.8	0.324	2165.2	0.103	0.039062	(.10)	0.2755	(.16)	0.05116	(.12)	**247.0**	**247.1**	**247.8**	0.649
z14(2)	ac	0.8	8.5	0.385	552.1	0.123	0.039053	(.37)	0.2755	(.55)	0.05116	(.39)	**247.0**	**247.1**	**248.3**	0.711
z(3)	ac	1.4	22.4	0.504	1376.9	0.160	0.039048	(.15)	0.2754	(.20)	0.05115	(.14)	**246.9**	**247.0**	**247.4**	0.735
z24	ac	0.6	26.7	0.543	1618.0	0.173	0.039023	(.16)	0.2753	(.29)	0.05117	(.23)	**246.8**	**246.9**	**248.3**	0.597
z(1)	ac	0.7	25.8	0.539	1563.5	0.171	0.039040	(.13)	0.2753	(.20)	0.05114	(.15)	**246.9**	**246.9**	**247.0**	0.665
z(4)	ac	1.0	27.5	0.612	1634.3	0.195	0.039029	(.13)	0.2752	(.20)	0.05115	(.15)	**246.8**	**246.9**	**247.6**	0.661
z22	ac	0.5	75.8	0.346	4807.5	0.110	0.039009	(.07)	0.2751	(.11)	0.05114	(.09)	**246.7**	**246.7**	**247.3**	0.619
z14	aa	0.5	13.7	0.406	869.2	0.129	0.038975	(.23)	0.2749	(.41)	0.05116	(.32)	**246.5**	**246.6**	**248.0**	0.623
z13	aa	0.4	14.3	0.478	888.1	0.153	0.038940	(.23)	0.2747	(.39)	0.05117	(.30)	**246.3**	**246.5**	**248.4**	0.634

z3	aa	0.4	21.4	0.458	1327.9	0.146	0.038918	(.16)	0.2745	(.24)	0.05115	(.18)	**246.1**	**246.3**	**247.8**	0.673
z18	ac	0.7	12.0	0.493	747.9	0.156	0.038937	(.28)	0.2743	(.57)	0.05109	(.47)	**246.2**	**246.1**	**245.0**	0.561
z4	aa	0.4	17.2	0.435	1074.2	0.140	0.038855	(.19)	0.2742	(.32)	0.05119	(.25)	**245.7**	**246.1**	**249.3**	0.635
z5	aa	0.9	7.7	0.365	502.7	0.120	0.038768	(.39)	0.2742	(.64)	0.05129	(.49)	**245.2**	**246.0**	**253.9**	0.652
z23	ac	0.7	18.8	0.999	1022.1	0.324	0.038786	(.25)	0.2739	(.46)	0.05122	(.37)	**245.3**	**245.8**	**250.5**	0.596
z8	aa	0.7	21.3	0.373	1355.7	0.119	0.038831	(.17)	0.2738	(.24)	0.05114	(.16)	**245.6**	**245.7**	**247.0**	0.743
z19	ac	1.1	7.8	0.246	522.7	0.085	0.036633	(.80)	0.2588	(.97)	0.05124	(.52)	**231.9**	**233.7**	**251.8**	0.845
PGD Tuff-1																
z7	aa	0.7	105.0	0.248	6582.5	0.105	0.101241	(.06)	0.9384	(.12)	0.06722	(.10)	**621.7**	**672.0**	**844.7**	0.514
z10	aa	2.0	11.1	0.297	683.8	0.152	0.079332	(.30)	0.7190	(.43)	0.06573	(.29)	**492.1**	**550.1**	**797.9**	0.729
z12	aa	1.6	10.9	0.282	680.1	0.147	0.062924	(.32)	0.5315	(.46)	0.06126	(.31)	**393.4**	**432.8**	**648.4**	0.741
z3	aa	0.5	64.9	0.157	4199.1	0.080	0.057746	(.10)	0.4727	(.14)	0.05937	(.10)	**361.9**	**393.1**	**580.6**	0.706
z5	aa	0.6	48.8	0.400	2936.7	0.170	0.054958	(.09)	0.4263	(.14)	0.05625	(.10)	**344.9**	**360.5**	**462.3**	0.698
z15b	aa	0.7	42.3	0.199	2761.0	0.078	0.043748	(.09)	0.3216	(.13)	0.05332	(.09)	**276.0**	**283.2**	**342.4**	0.695
z8	aa	0.8	54.2	0.227	3519.4	0.084	0.040122	(.07)	0.2888	(.12)	0.05220	(.09)	**253.6**	**257.6**	**294.2**	0.650
z13	aa	0.7	24.5	0.329	1567.0	0.110	0.039384	(.16)	0.2796	(.24)	0.05148	(.18)	**249.0**	**250.3**	**262.5**	0.665
z9	aa	0.6	37.7	0.275	2445.9	0.088	0.039239	(.09)	0.2772	(.16)	0.05124	(.13)	**248.1**	**248.4**	**251.6**	0.617
z22b	ac	0.8	27.7	0.277	1802.1	0.089	0.039202	(.12)	0.2768	(.19)	0.05121	(.15)	**247.9**	**248.1**	**250.4**	0.630
z(4)	ac	0.6	82.9	0.253	5386.9	0.081	0.039134	(.06)	0.2763	(.11)	0.05120	(.09)	**247.5**	**247.7**	**250.1**	0.542
z(5)	ac	0.5	83.5	0.372	5250.3	0.119	0.039140	(.06)	0.2762	(.10)	0.05119	(.08)	**247.5**	**247.7**	**249.3**	0.622
z(3)	ac	0.6	54.9	0.366	3460.7	0.117	0.039120	(.08)	0.2762	(.13)	0.05120	(.10)	**247.4**	**247.6**	**249.9**	0.631
z(2)	ac	1.2	59.9	0.618	3531.6	0.199	0.039105	(.07)	0.2761	(.11)	0.05121	(.08)	**247.3**	**247.6**	**250.4**	0.652
z(9)	ac	1.5	22.1	0.544	1339.2	0.174	0.039113	(.15)	0.2761	(.22)	0.05119	(.15)	**247.3**	**247.5**	**249.4**	0.714
z17b	aa	0.5	45.5	0.347	2884.1	0.112	0.039061	(.09)	0.2759	(.14)	0.05123	(.11)	**247.0**	**247.4**	**251.3**	0.653
z(6)	ac	0.7	42.2	0.337	2689.2	0.107	0.039104	(.09)	0.2758	(.18)	0.05115	(.15)	**247.3**	**247.3**	**247.8**	0.568
z16b	aa	0.4	79.8	0.282	5145.9	0.090	0.039075	(.06)	0.2758	(.11)	0.05119	(.09)	**247.1**	**247.3**	**249.4**	0.588

z4	aa	0.5	24.0	0.355	1529.6	0.113	0.039086	(.13)	0.2757	(.22)	0.05115	(.17)	**247.2**	**247.2**	**247.8**	0.648
z2	aa	0.8	20.5	0.306	1325.6	0.097	0.039082	(.15)	0.2756	(.21)	0.05115	(.15)	**247.1**	**247.2**	**247.7**	0.720
z14b	aa	0.4	28.4	0.343	1812.0	0.110	0.039022	(.12)	0.2753	(.22)	0.05116	(.17)	**246.8**	**246.9**	**248.2**	0.604
z18b	aa	1.2	17.0	0.357	1091.6	0.114	0.038653	(.18)	0.2723	(.28)	0.05110	(.20)	**244.5**	**244.6**	**245.3**	0.698
z20b	aa	0.8	16.7	0.710	973.1	0.229	0.038592	(.20)	0.2723	(.31)	0.05117	(.22)	**244.1**	**244.5**	**248.5**	0.691
PGD Tuff-2																
z27b	ac	1.5	18.9	0.088	1135.6	0.108	0.093920	(.29)	1.7667	(.31)	0.13643	(.10)	**578.7**	**1033.3**	**2182.4**	0.945
z28b	ac	0.5	157.8	0.059	9889.2	0.075	0.064534	(.05)	0.8664	(.07)	0.09737	(.05)	**403.1**	**633.6**	**1574.3**	0.716
z25b	aa	2.0	26.1	0.175	1646.2	0.110	0.069850	(.15)	0.6548	(.16)	0.06799	(.05)	**435.2**	**511.4**	**868.2**	0.947
z10	aa	0.6	40.8	0.186	2599.8	0.095	0.071192	(.18)	0.6202	(.26)	0.06319	(.18)	**443.3**	**490.0**	**714.5**	0.714
z23b	aa	3.3	8.8	0.108	572.6	0.091	0.059677	(.25)	0.5930	(.30)	0.07207	(.15)	**373.7**	**472.8**	**987.8**	0.873
z6	aa	0.6	62.9	0.641	3442.0	0.285	0.069712	(.11)	0.5793	(.16)	0.06027	(.12)	**434.4**	**464.0**	**613.3**	0.711
z1	aa	0.7	30.0	0.149	1949.5	0.080	0.051935	(.11)	0.4202	(.21)	0.05868	(.17)	**326.4**	**356.2**	**555.4**	0.588
z16	aa	0.9	33.6	0.182	2180.6	0.083	0.045743	(.12)	0.3472	(.23)	0.05505	(.19)	**288.3**	**302.6**	**414.1**	0.575
z12	aa	1.1	20.6	0.268	1335.8	0.095	0.042629	(.33)	0.3079	(.37)	0.05238	(.16)	**269.1**	**272.5**	**302.0**	0.897
z8	aa	0.8	91.6	0.242	5929.9	0.084	0.040452	(.07)	0.2893	(.12)	0.05187	(.09)	**255.6**	**258.0**	**279.5**	0.594
z(2)	ac	1.5	9.2	0.521	565.2	0.175	0.040252	(.35)	0.2867	(.61)	0.05165	(.48)	**254.4**	**255.9**	**270.0**	0.615
z5	aa	0.6	44.0	0.290	2815.8	0.102	0.039744	(.09)	0.2840	(.18)	0.05182	(.15)	**251.2**	**253.8**	**277.5**	0.573
z(5)	ac	0.6	70.6	0.260	4584.8	0.083	0.039282	(.06)	0.2773	(.09)	0.05120	(.07)	**248.4**	**248.5**	**249.7**	0.687
z(6)	ac	0.8	53.2	0.401	3323.9	0.129	0.039253	(.07)	0.2772	(.13)	0.05123	(.10)	**248.2**	**248.5**	**251.0**	0.598
z(8)	ac	0.6	92.2	0.226	6035.4	0.072	0.039223	(.06)	0.2770	(.09)	0.05122	(.07)	**248.0**	**248.3**	**250.6**	0.617
z4	aa	0.9	16.7	0.348	1073.2	0.111	0.039220	(.19)	0.2768	(.27)	0.05118	(.19)	**248.0**	**248.1**	**249.0**	0.720
z2	aa	0.6	48.4	0.302	3112.7	0.096	0.039194	(.08)	0.2766	(.13)	0.05119	(.11)	**247.8**	**248.0**	**249.2**	0.597
z11	aa	0.6	11.7	0.522	722.5	0.169	0.039116	(.29)	0.2765	(.47)	0.05126	(.36)	**247.4**	**247.9**	**252.7**	0.653
z3	aa	0.6	13.6	0.555	828.2	0.177	0.039146	(.23)	0.2763	(.38)	0.05119	(.29)	**247.5**	**247.7**	**249.3**	0.654
z(1)	ac	1.0	24.7	0.354	1574.5	0.113	0.039146	(.13)	0.2762	(.17)	0.05118	(.10)	**247.5**	**247.7**	**248.7**	0.776

z(4)	ac	0.7	60.1	0.764	3418.2	0.244	0.039126	(.10)	0.2761	(.20)	0.05118	(.17)	**247.4**	**247.6**	**249.0**	0.523
z(10)	ac	0.2	202.0	0.367	12700.5	0.117	0.039117	(.05)	0.2760	(.09)	0.05117	(.08)	**247.4**	**247.5**	**248.5**	0.569
z(3)	ac	0.8	49.0	0.394	3069.2	0.126	0.039110	(.08)	0.2760	(.14)	0.05118	(.11)	**247.3**	**247.5**	**248.8**	0.598
z(7)	ac	0.6	30.1	0.541	1821.2	0.173	0.039084	(.13)	0.2759	(.22)	0.05120	(.18)	**247.2**	**247.4**	**249.8**	0.603
z7	aa	0.9	28.8	0.381	1816.7	0.122	0.039075	(.12)	0.2758	(.20)	0.05120	(.15)	**247.1**	**247.3**	**249.7**	0.634
z(9)	ac	0.6	103.9	0.436	6418.3	0.139	0.039100	(.17)	0.2758	(.22)	0.05116	(.13)	**247.2**	**247.3**	**248.2**	0.799
z18	aa	1.0	13.7	0.496	847.2	0.159	0.039055	(.23)	0.2756	(.36)	0.05118	(.27)	**247.0**	**247.2**	**249.0**	0.680
z20	aa	0.9	10.9	0.546	670.5	0.173	0.039072	(.29)	0.2755	(.41)	0.05114	(.28)	**247.1**	**247.1**	**247.0**	0.730
z9	aa	0.9	30.0	0.346	1911.1	0.113	0.038653	(.11)	0.2730	(.19)	0.05123	(.15)	**244.5**	**245.1**	**251.1**	0.621
PGD Tuff-3																
z4	aa	1.3	5.6	0.222	380.6	0.072	0.062038	(.97)	0.4674	(1.28)	0.05464	(.80)	**388.01**	**389.39**	**397.6**	0.780
z(13)	ac	0.2	72.6	0.094	4781.1	0.058	0.049106	(.07)	0.4065	(.14)	0.06003	(.12)	**309.03**	**346.33**	**604.8**	0.553
z6	aa	1.3	5.2	0.217	351.5	0.086	0.040359	(1.03)	0.2935	(1.16)	0.05274	(.51)	**255.06**	**261.31**	**317.7**	0.900
z3	aa	0.7	13.3	0.234	876.8	0.086	0.040619	(.22)	0.2927	(.33)	0.05227	(.23)	**256.67**	**260.71**	**297.2**	0.704
z(14)	ac	0.2	54.1	0.417	3364.2	0.134	0.040113	(.07)	0.2841	(.16)	0.05136	(.14)	**253.53**	**253.88**	**257.1**	0.493
z2	aa	1.0	5.5	0.287	368.6	0.095	0.039826	(1.29)	0.2829	(1.35)	0.05151	(.39)	**251.76**	**252.93**	**263.9**	0.958
z(12)	ac	0.3	43.2	0.263	2799.7	0.087	0.039738	(.08)	0.2821	(.14)	0.05149	(.11)	**251.21**	**252.33**	**262.8**	0.609
z(3)	ac	0.3	162.7	0.456	9972.6	0.147	0.039182	(.05)	0.2768	(.10)	0.05123	(.09)	**247.76**	**248.09**	**251.2**	0.528
z(17)	ac	1.4	35.7	0.464	2199.3	0.149	0.039122	(.21)	0.2762	(.23)	0.05120	(.10)	**247.39**	**247.62**	**249.8**	0.912
z(5)	ac	1.3	17.8	0.333	1143.8	0.106	0.039142	(.17)	0.2762	(.23)	0.05117	(.15)	**247.51**	**247.62**	**248.6**	0.759
z(4)	ac	0.5	140.7	0.303	9003.6	0.097	0.039079	(.05)	0.2758	(.08)	0.05119	(.06)	**247.12**	**247.32**	**249.2**	0.644
z(10)	ac	0.3	21.3	0.535	1298.0	0.170	0.039098	(.16)	0.2758	(.35)	0.05116	(.30)	**247.24**	**247.31**	**247.9**	0.522
z(9)	ac	0.3	77.0	0.517	4665.8	0.164	0.039098	(.06)	0.2757	(.11)	0.05114	(.09)	**247.24**	**247.24**	**247.2**	0.568
z(2)	ac	0.2	173.3	0.532	10425.6	0.169	0.039083	(.06)	0.2757	(.09)	0.05116	(.07)	**247.15**	**247.23**	**248.0**	0.688
z(15)	ac	0.5	33.7	0.513	2050.5	0.163	0.039064	(.10)	0.2754	(.19)	0.05114	(.15)	**247.03**	**247.02**	**247.0**	0.590
z(8)	ac	0.4	68.3	0.517	4141.0	0.164	0.039046	(.06)	0.2753	(.13)	0.05114	(.11)	**246.92**	**246.95**	**247.3**	0.531

z(11)	ac	0.8	25.9	0.565	1561.2	0.181	0.039001	(.13)	0.2753	(.18)	0.05119	(.13)	**246.64**	**246.90**	**249.4**	0.717
z(6)	ac	0.3	57.8	0.656	3380.3	0.208	0.039003	(.07)	0.2750	(.13)	0.05114	(.11)	**246.65**	**246.68**	**247.0**	0.567
z(1)	ac	0.3	61.6	0.587	3667.8	0.187	0.038983	(.12)	0.2749	(.17)	0.05114	(.12)	**246.52**	**246.60**	**247.3**	0.732
z(7)	ac	0.3	33.8	1.088	1794.8	0.344	0.038847	(.12)	0.2736	(.20)	0.05108	(.16)	**245.68**	**245.58**	**244.6**	0.620

(a) All analyses are single zircon grains. Data used in age calculations are in bold. aa = air-abraded, ca = annealed and chemically treated.
(b) Pb_c is total common Pb in analysis. Pb* is radiogenic Pb concentration.
(c) Measured ratio corrected for spike and fractionation only.
(d) Radiogenic Pb ratio.
(e) Corrected for fractionation, spike, blank, and initial common Pb.
Mass fractionation correction of 0.25%/amu ± 0.04%/amu (atomic mass unit) was applied to single-collector Daly analyses.
Total procedural blank averaged ca. 0.7 pg for Pb and less than 0.1 pg for U.
Blank isotopic composition: 206Pb/204Pb = 18.27 ± 0.1, 207Pb/204Pb =15.59 ± 0.1, 208Pb/204Pb = 38.12 ± 0.1.
Corr. coef. = correlation coefficient.
Age calculations are based on the decay constants of Jaffey et al. (1971).

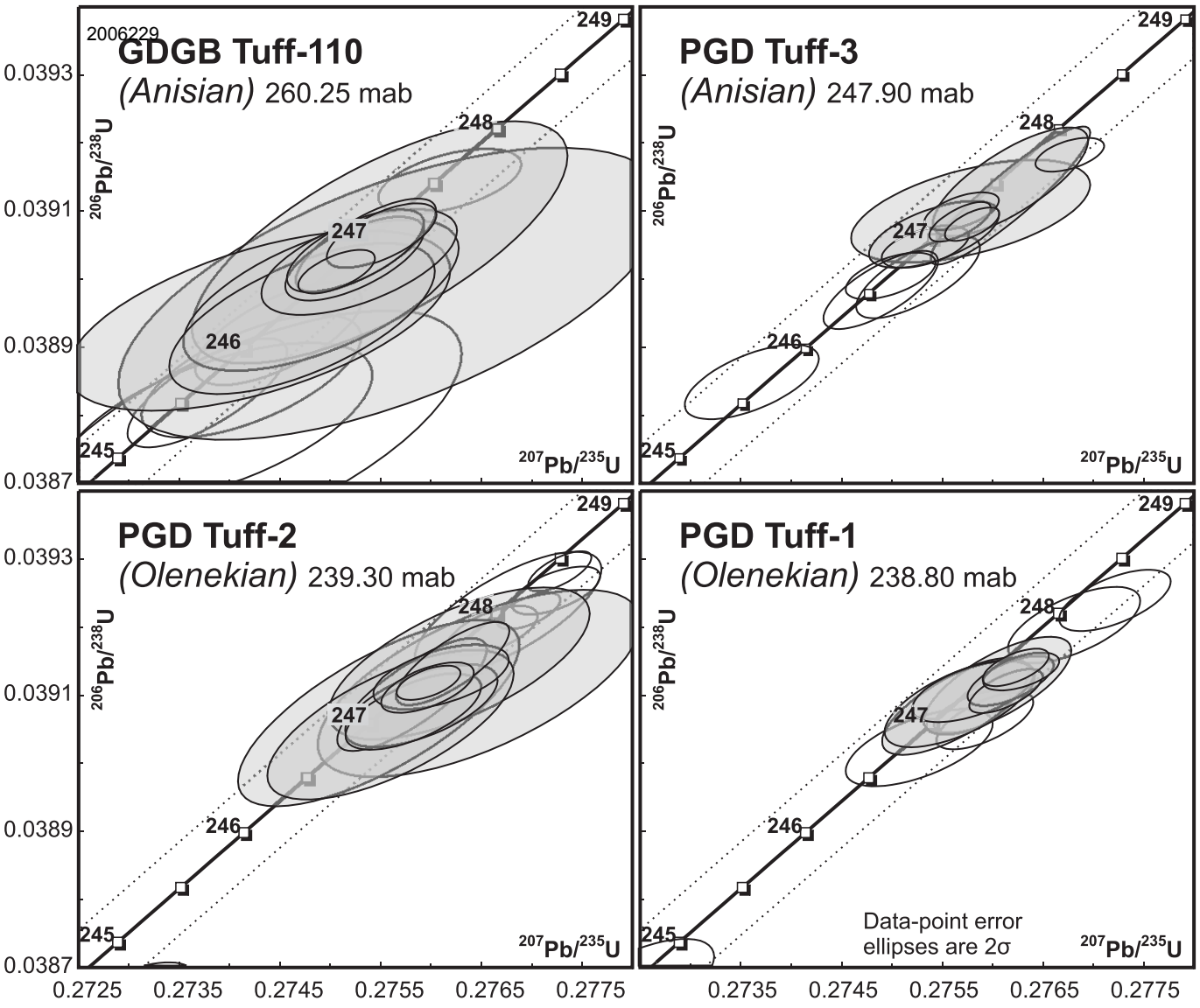

Figure DR1 (Lehrmann et al.) Conventional concordia diagrams for U-Pb single zircon analyses from the Olenekian-Anisian boundary ash beds at Guandao section (stratigraphic positions and age estimates shown in figure 2). Analyses selected for weighted mean calculation are shaded. Dotted lines depict uncertainity in the U decay constants. Sample elevations in meters above base of section given (mab, see figure 2). Not all analyses are shown in the plots (see Table DR1 for the complete data).

Figure DR2 (below). Magnetostratigraphic results from the Guandao section. From right to left, the diagram shows height, NRM intensity, declination, inclination, VGP latitude of the ChRM of all data that meet the reliability criteria defined in text, magnetic polarity, maximum angle of deviation (MAD), demagnetization temperature range that defined the ChRM and the number of demagnetization vectors that define the ChRM. Tick marks next to 'height' indicate location of paleomagnetic sample. Grey shading indicates stratigraphic position of breccia interval (instantaneous debris flows), brown shading indicates stratigraphic position of shale and green shading indicates covered section. Gaps in polarity record are marked by a cross. Un-sampled breccia intervals are not regarded as gaps in the polarity record due to the geologically instantaneous nature of their deposition. Normal polarity is indicated by black and reverse polarity by white in the magnetic polarity column. Stratigraphic elevations are different than those shown in Figure 2 (offset 11.4 m lower).This resulted because the Guandao section has been re-measured several times. Stratigraphic elevations given in figure 2 are from the original measured section which we consider most accurate for placement of litholofacies boundaries. The elevations in figures DR2 and DR3 were obtained during re-measurement for paleomagnetic sampling which started the base of the section several meters lower than the original section. Although stratigraphic elevations differ, all sampling is precisely tied between the section in figures 2 and DR2/3 because paleomagnetic samples and conodont samples were taken from the same beds numbered in outcrop, and geochronology samples were taken in the context of the numbered beds.

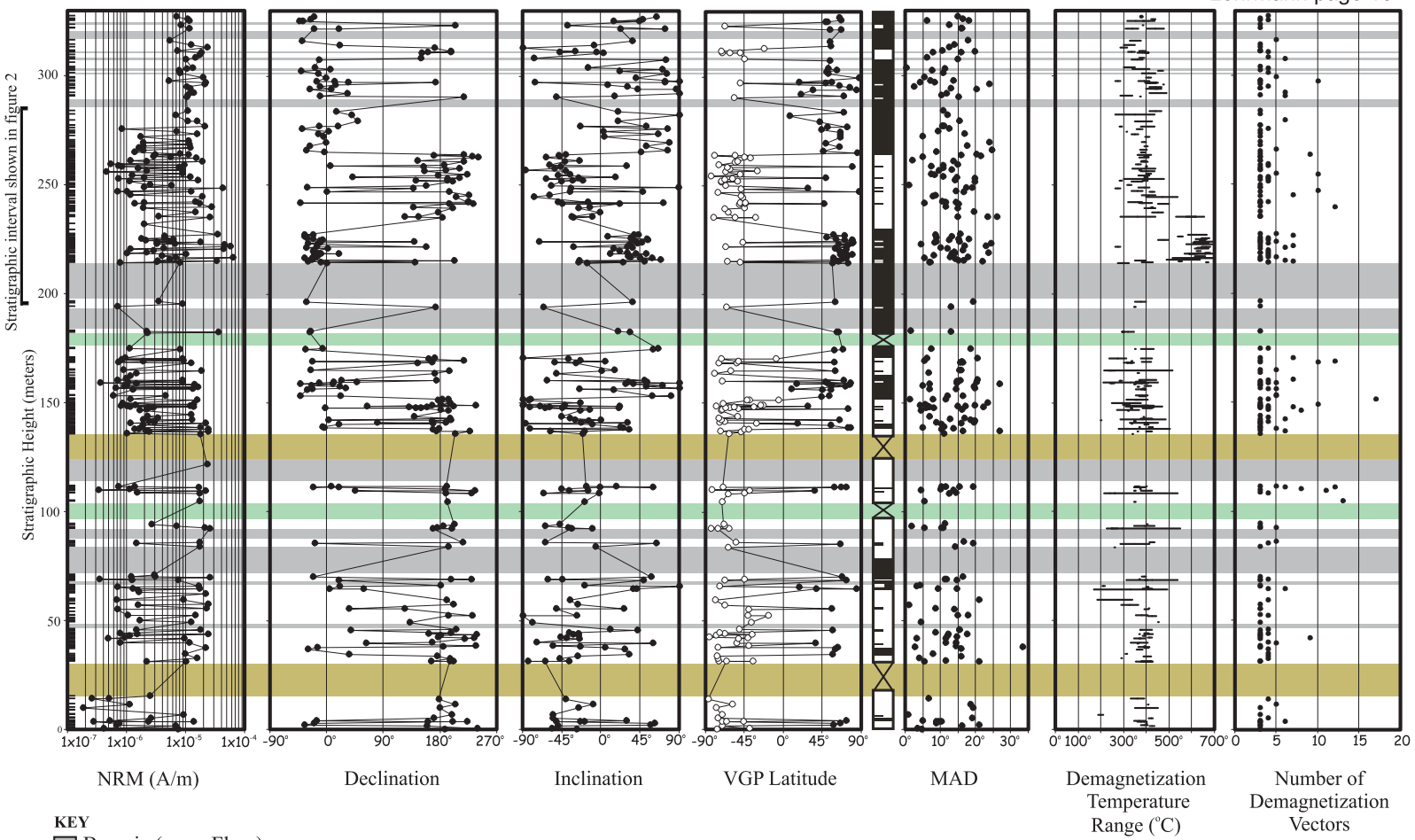

KEY

- Breccia (mass Flow)
- Shale
- Covered Section
- Normal Polarity
- Reverse Polarity
- Polarity Record Gap (covered Section)
- Polarity Record Gap (shale)

Figure DR2 (Lehrmann et al.)

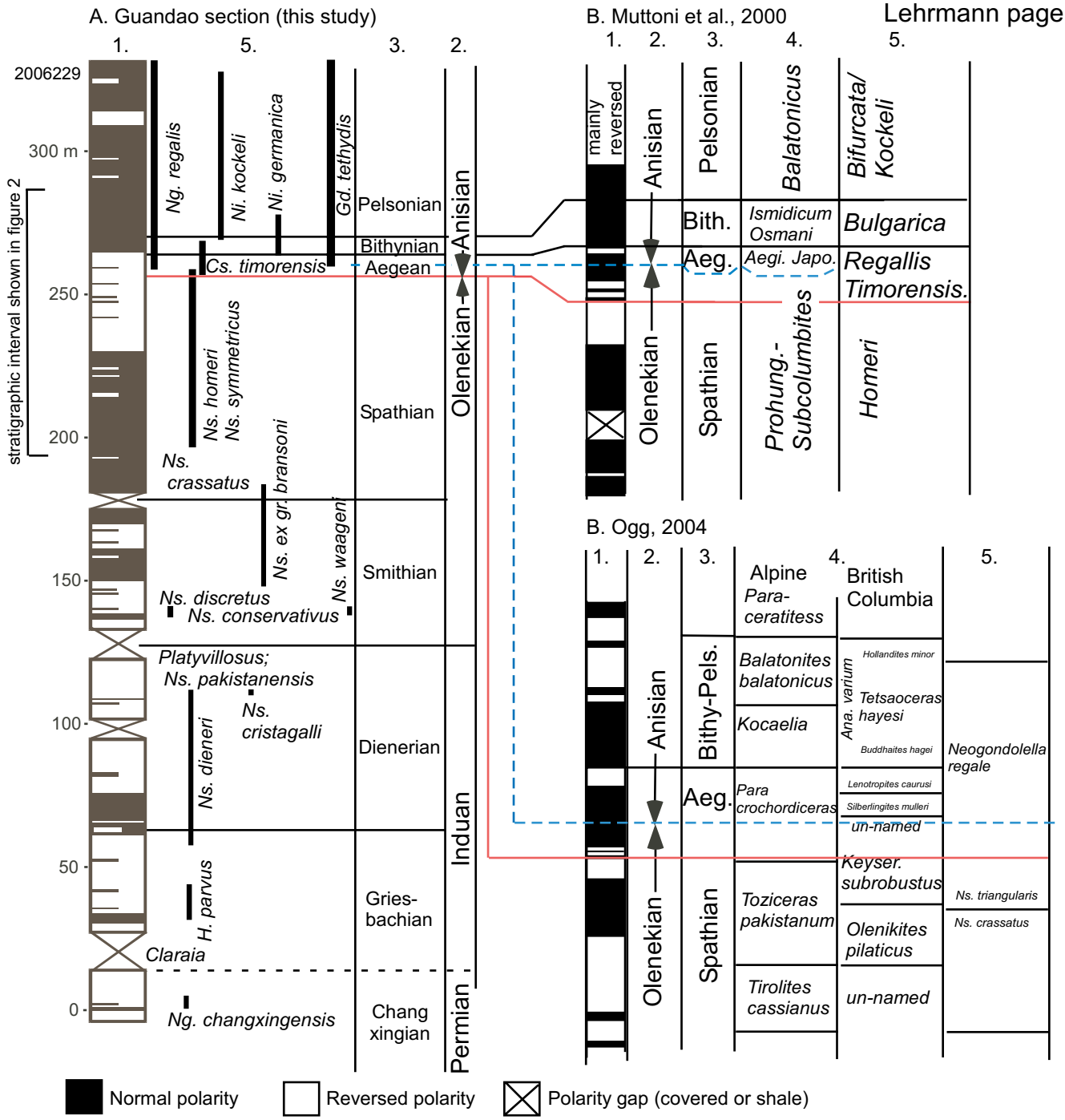

Figure DR3 (Lehrmann et al.) **A.** Magnetic reversal stratigraphy and biostratigraphic ranges of important conodonts from Guandao section. Section spans Upper Permian through Middle Anisian Pelsonian. Permian-Triassic boundary is placed at contact between Dalong Formation bearing *Ng. changxingensis* and overlying shale bearing the bivalve *Claraia*. The soft shale in the basal Triassic was impossible to sample for paleomagnetic measurements, and may be hiding a normal polarity zone that is typically found in the base of the Triassic (cf. Steiner et al.,1989; Ogg, 2004). Olenekian-Anisian boundary is placed on the basis of the first appearance of *Cs. timorensis*. **B.** Correlation of magnetic reversal stratigraphy of Guandao section with composite section of Muttoni et al. (2000) and Ogg (2004). Red correlation line is O-A boundary defined on basis of conodonts. Blue dashed correlation line is O-A boundary defined on basis of ammonoids. Note the conodont datum places the O-A boundary slightly lower in Guandao section than the ammonoid defined boundary in the Muttoni et al. (2000) and Ogg (2004) compilations. Column headings as follows: 1. polarity zone, 2. stage, 3. substage, 4. ammonoid zones, 5. conodont zones.

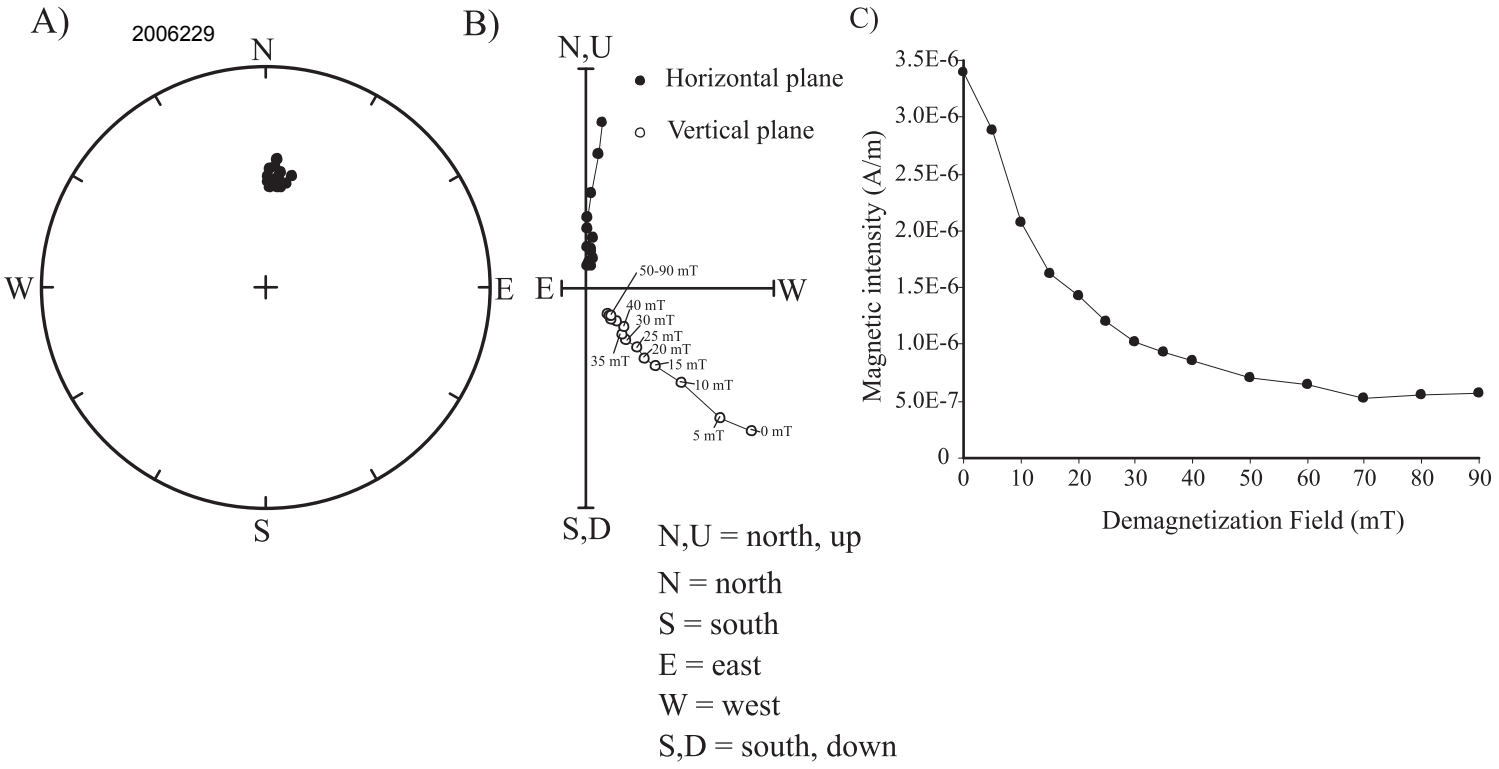

Figure DR4 (Lehrmann et al.) Equal area stereographic projection (**A**), Zijderveld plot (**B**) of AF demagnetization vectors in geographic coordinates and demagnetization plot (**C**) for a representative sample from the Guandao section, Guizhou, south China. Solid circles on the stereoplots are directions in the lower hemisphere. Filled circles on the Zijderveld plots are projections onto a horizontal plane with north oriented to the top and open circle are projections onto a north-south vertical plane. This example shows a northerly downward-directed component being removed during AF demagnetization step. This downward vector corresponds approximately to the current dipole or recent geomagnetic field direction.

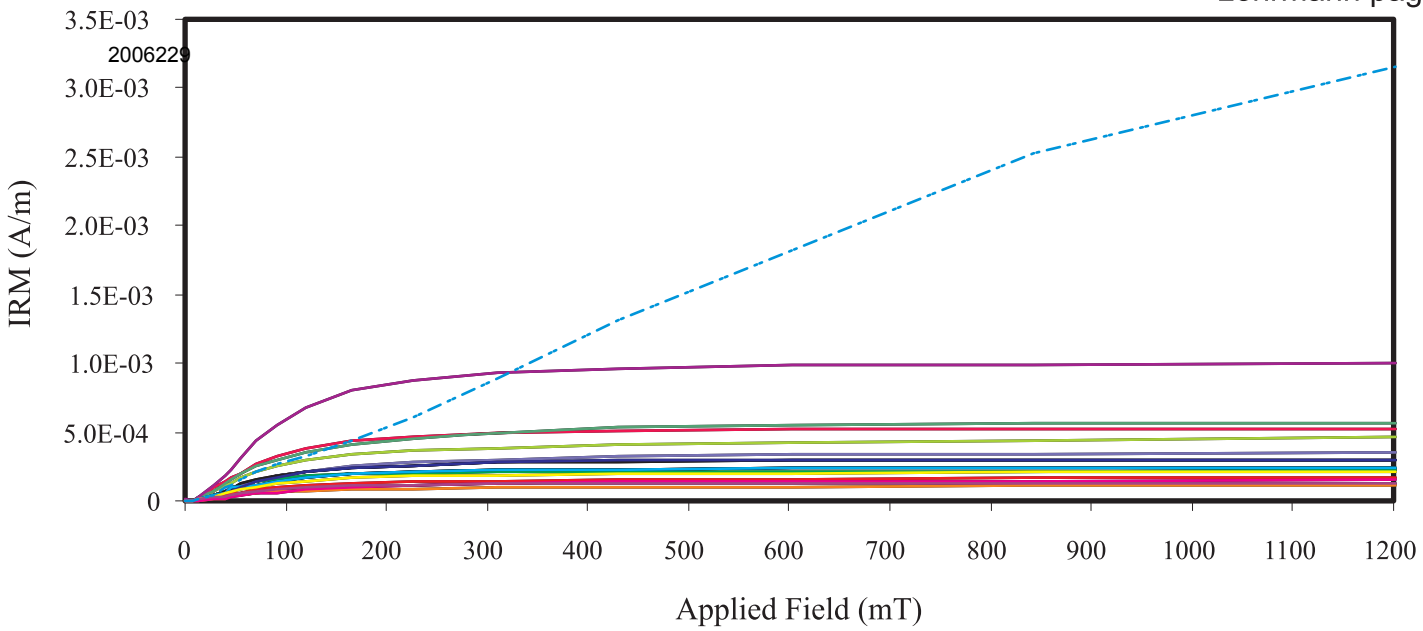

Figure DR5 . Isothermal Remanent Magnetization (IRM) acquisition curves for 18 representative limestone samples from the Guandao section. Approximately 61% (n = 11) of the specimens became magnetically saturated at low applied magnetic fields yielding $IRM_{0.3T}/IRM_{1.2T}$ ratio values of 0.9 or above. The remaining specimens yielded $IRM_{0.3T}/IRM_{1.2T}$ ratio values of 0.8 or above for 33 % (n = 6) of the data set and less than 0.3 for 5% (n = 1) of the data set.

Figure DR6 (Below). Typical IRM acquisition and thermal demagnetization behavior for representative samples of limestone from the Guandao section. Acquisition curves are shown in green lines with green triangle symbols. Thermal demagnetization of three orthogonal components (0.0.2, 0.2-0.4, and 0.4-1.2 T) is plotted for each of the three examples. Magnetic susceptibility after each thermal demagnetization step is also plotted in orange. Example A) consists of a specimen of dark-grey deep water limestone and exhibits two unblocking temperatures at 340^{o}c and 575^{o}C. The lower unblocking temperature results in the removal of the soft and medium IRM. The most stable (hard) IRM is removed at 575^{o}C. Magnetic susceptibility begins to rise at temperatures between 475-550^{o}C indicating the formation of new magnetic mineral phases. Example B) consists of a second specimen of dark-grey deep water limestone and exhibits two unblocking temperatures at 325^{o}c and 550^{o}C. The lower unblocking temperature results in the removal of the soft and medium IRM. The most stable (hard) IRM is removed at 550^{o}C. However, magnetic susceptibility begins to rise at temperatures between 400-450^{o}C indicating the formation of new magnetic mineral phases. Example C) consists of a specimen of pinkish-grey limestone and exhibits only one unblocking temperature between 650-675^{o}C. This unblocking temperature results in the removal of the soft, medium and hard IRM. Magnetic susceptibility begins to rise at temperatures between 475-525^{o}C indicating the formation of new magnetic mineral phases.

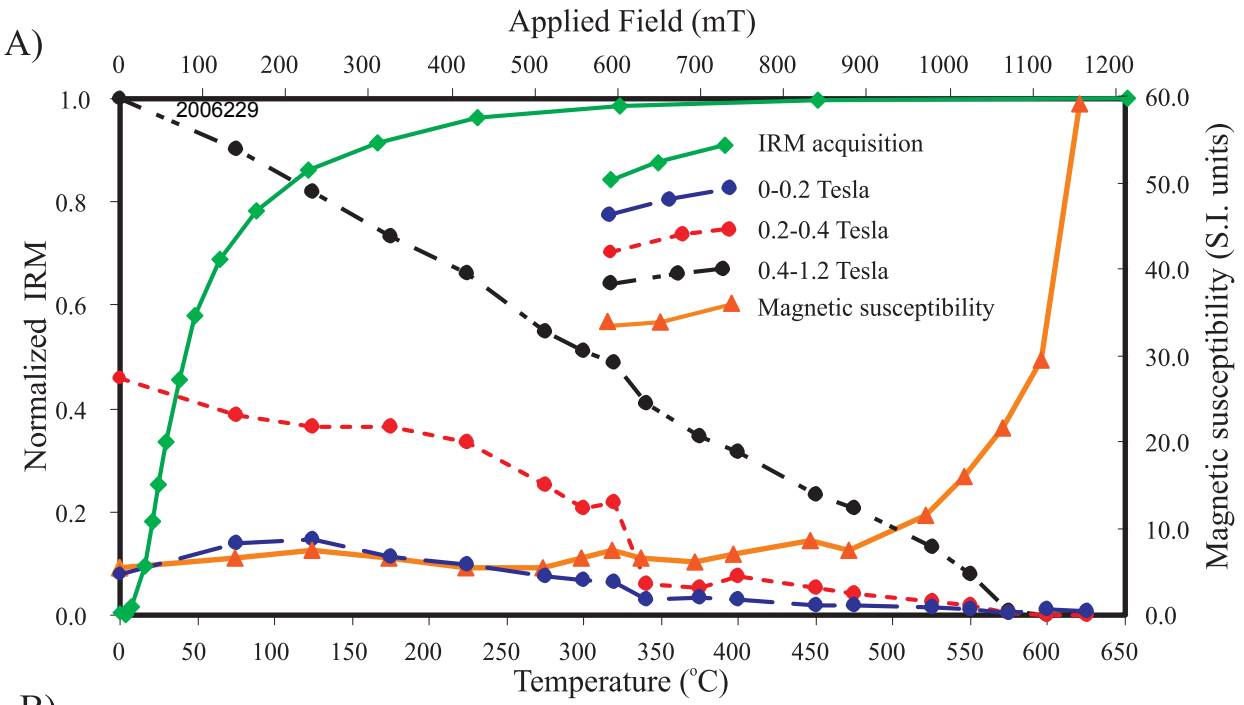

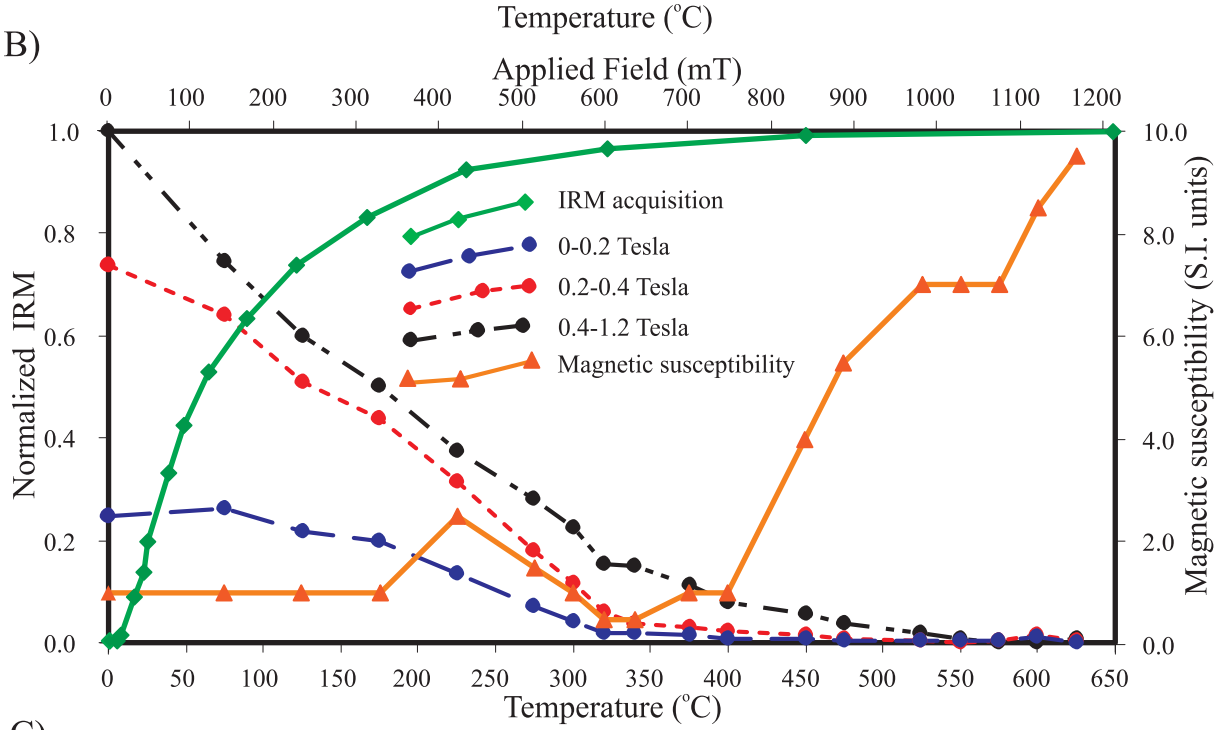

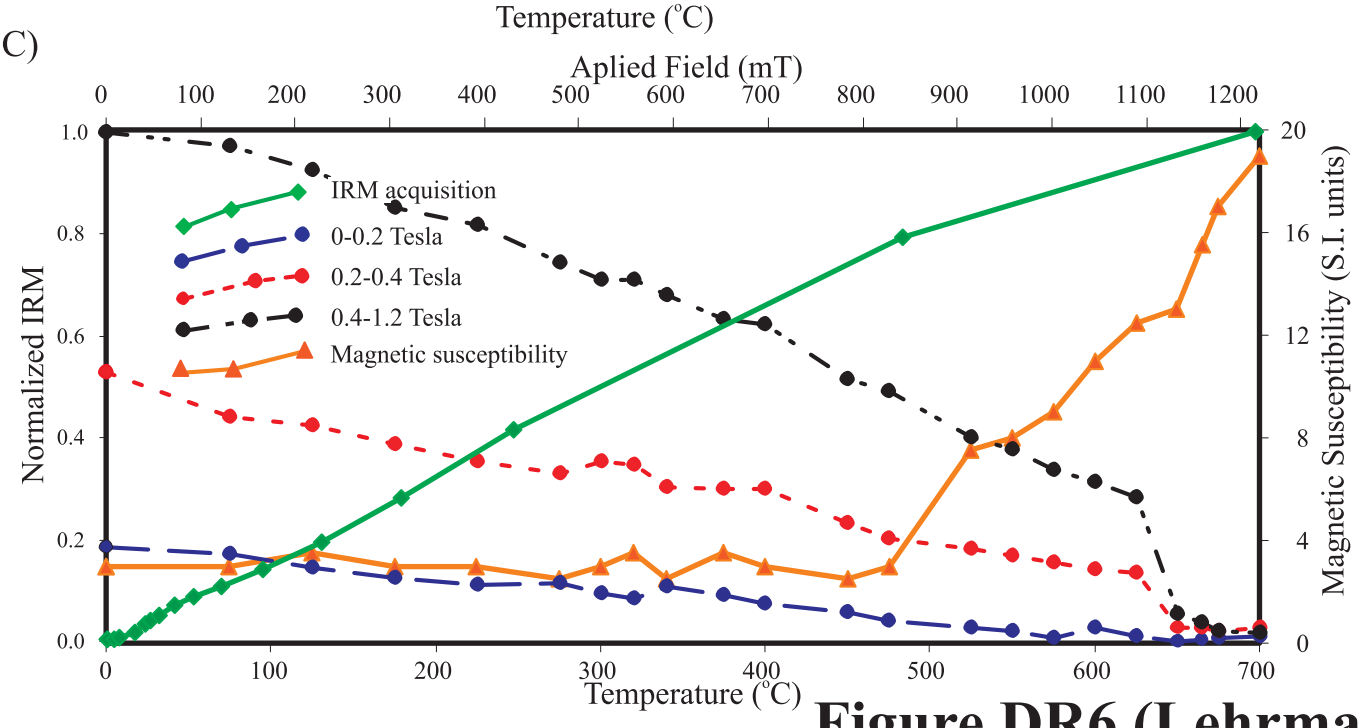

Figure DR6 (Lehrmann et al.)

Figure DR7 (below). Examples of typical demagnetization experiments on specimens collected from the Guandao section. (A) Normal-polarity sample M116-B collected at a stratigraphic height of 215.8 m; (B) Reverse-polarity sample M34-B collected at a stratigraphic height of 57.2 m; (C) Reverse-polarity sample M77-B collected at a stratigraphic height of 146.4 m and (D) Normal-polarity sample M180-B collected at a stratigraphic height of 260 m. The figures show from left to right: (i) equal area stereographic projection of demagnetization vectors in geographic coordinates; solid circles are directions in the lower hemisphere of the projection; open circles are directions in the upper hemisphere; (ii) equal area stereographic projection of demagnetization vectors in stratigraphic coordinates; (iii) z-plot of demagnetization in stratigraphic coordinates; filled circles are projections of vectors onto the horizontal plane with north oriented to the top; open circles are projections onto a north south vertical plane; and (iv) magnetic intensity-temperature plot.

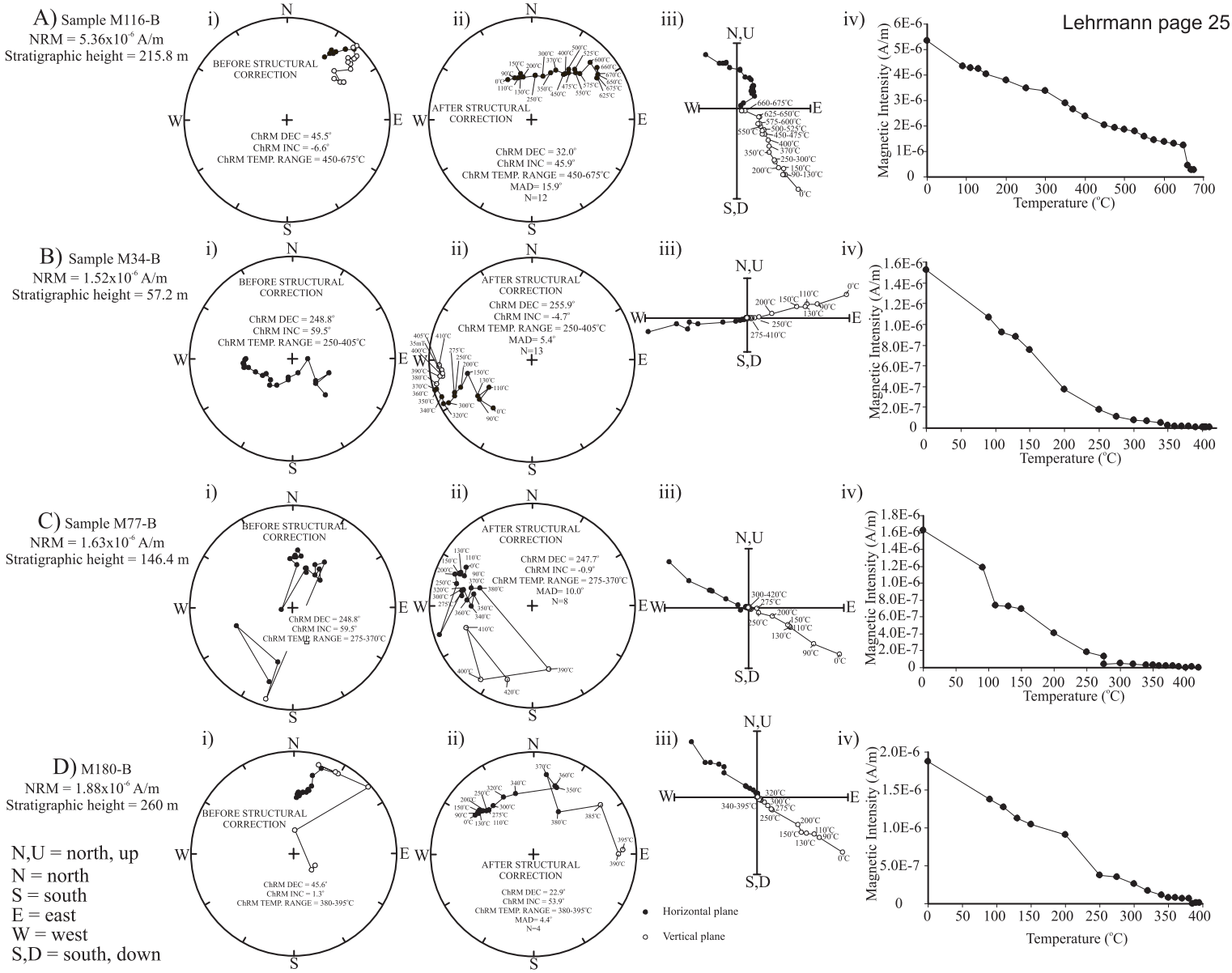

Figure DR7 (Lehrmann et al.)

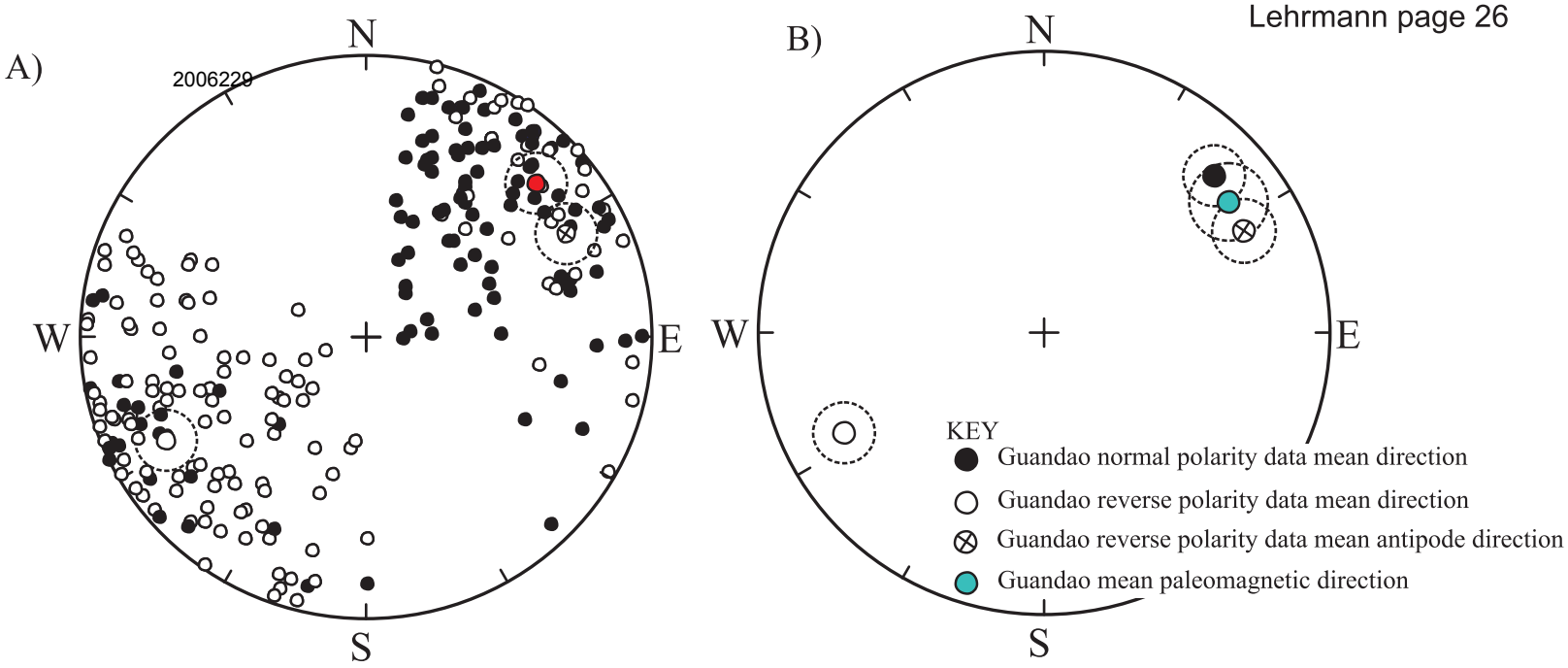

Figure DR8 (Lehrmann et al.) Equal area stereographic projection of : (**A**) site mean ChRM directions from 243 sites at Guandao section; solid circles are directions in the lower hemisphere of the projection; open circles are directions in the upper hemisphere; the mean of the 118 normal polarity sites is shown by a red circle with surrounding circle of 95% confidence limit (D = 47.8°, I = 19.6°, R = 95.1, $_{95}$ = 10.8°, k = 5.1); the mean of the 125 reverse polarity sites is shown by a white circle with surrounding circle of 95% confidence limit (D = 242.5°, I = -22.0°, R = 101.9, $_{95}$ = 8.3°, k = 5.4); the antipode of the mean of the reverse polarity sites is shown by a white circle and cross with surrounding circle of 95% confidence limit (D = 47.8°, I = 19.6°). (**B**) the comparison between the Guandao section site mean ChRM normal polarity paleomagnetic direction (with surrounding circle of 95% confidence limit) with the antipodal Guandao section site mean ChRM reverse polarity paleomagnetic direction (with surrounding circle of 95% confidence limit) and the mean ChRM normal polarity of all directions from 243 sites at Guandao section (with surrounding circle of 95% confidence limit). The mean of the 125 reverse polarity sites is shown by a white circle with surrounding circle of 95% confidence limit is shown for reference.

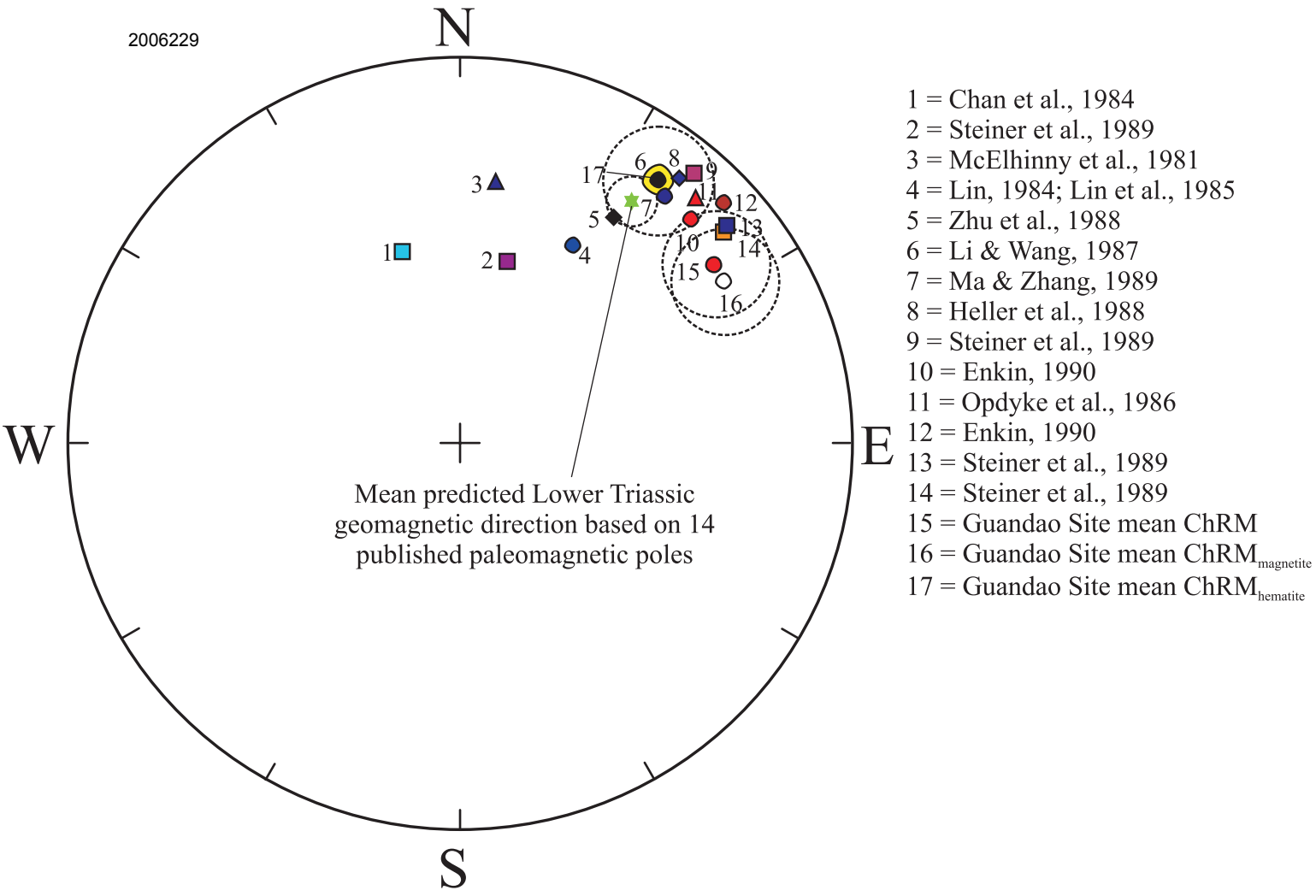

Figure DR9 (Lehrmann et al.) Equal area stereographic projection comparing the predicted direction for the Guandao locality based on published Lower Triassic paleomagnetic poles (1-14) for the South China Block and a mean predicted Lower Triassic geomagnetic direction based on those 14 published paleomagnetic poles (green star with surrounding circle of 95% confidence limit) with the Guandao site mean ChRM direction (this study), the Guandao magnetite site mean ChRM direction (this study) and the Guandao site mean hematite ChRM direction (this study).

Figure DR10 (below). Equal area stereographic projection of: (**A**) Site mean hematite ChRM directions from 25 sites at Guandao section; solid circles are directions in the lower hemisphere of the projection; open circles are directions in the upper hemisphere; the mean of the 21 normal polarity sites is shown by a green circle with surrounding circle of 95% confidence limit (D = 37.0°, I = 16.2°, $\forall_{95}$ =5.6°, R = 20.0, k = 19.1); the mean of the 4 reverse polarity sites is shown by a white circle with surrounding circle of 95% confidence limit (D = 191.8°, I = -12.2°, $\forall_{95}$ =24.6°, R = 3.7, k = 1.0); the antipode of the mean of the reverse polarity sites is shown by a white circle and cross with surrounding circle of 95% confidence limit (D = 11.8°, I = 12.2°). (**B**) Site mean magnetite ChRM directions from 218 sites at Guandao section; the mean of the 97 normal polarity sites is shown by a blue circle with surrounding circle of 95% confidence limit (D = 50.7°, I = 20.3°, $\forall_{95}$ =11.5°, R = 75.6, k = 4.5); the mean of the 121 reverse polarity sites is shown by a white circle with surrounding circle of 95% confidence limit (D = 244.2°, I = -22.1°, $\forall_{95}$ =10.3°, R = 99.5, k = 5.6); the antipode of the mean of the reverse polarity sites is shown by a white circle and cross with surrounding circle of 95% confidence limit (D = 64.2°, I = 22.1°). (**C**) Site mean hematite ChRM directions from 25 sites (reverse polarity directions inverted) at Guandao section (D = 33.1°, I = 15.8°, $\forall_{95}$ =4.9°, R = 23.3, k = 24.4) is shown by a green circle with surrounding circle of 95% confidence. (**D**) Site mean magnetite ChRM directions from 218 sites (reverse polarity directions inverted) at Guandao section (D = 58.3°, I = 21.5°, $\forall_{95}$ =11.0°, R = 174.0, k = 4.9) is shown by a blue circle with surrounding circle of 95% confidence. (**E**) Comparison of mean site magnetite ChRM directions (solid blue circle) from 218 sites (reverse polarity directions inverted) at Guandao section (with surrounding circle of 95% confidence limit) with mean site hematite ChRM directions (solid green circle) from 25 sites (reverse polarity directions inverted) at Guandao section (with surrounding circle of 95% confidence limit). Statistically these two directions are not the same at a 95% confidence level.

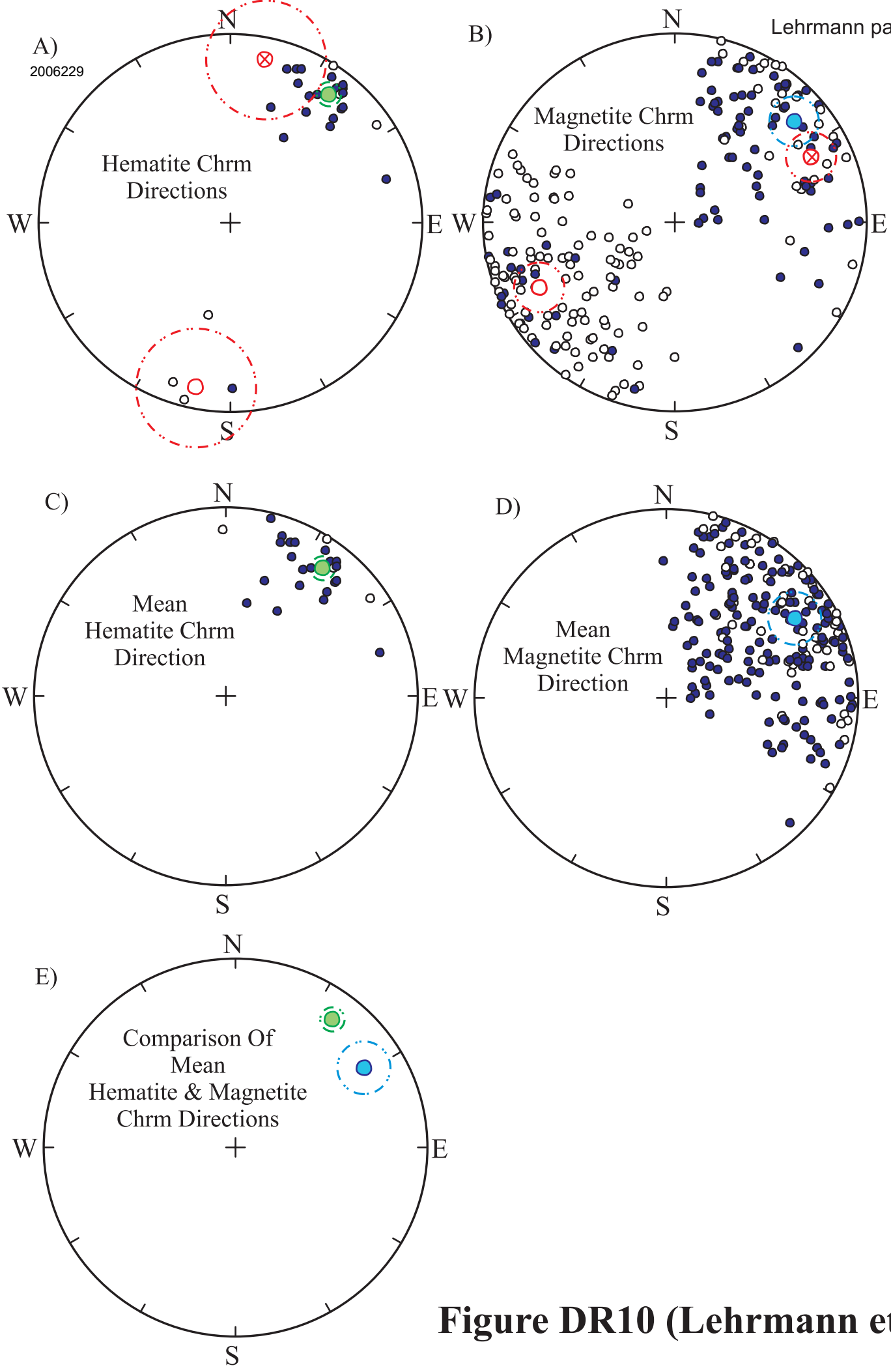

Figure DR10 (Lehrmann et al.)

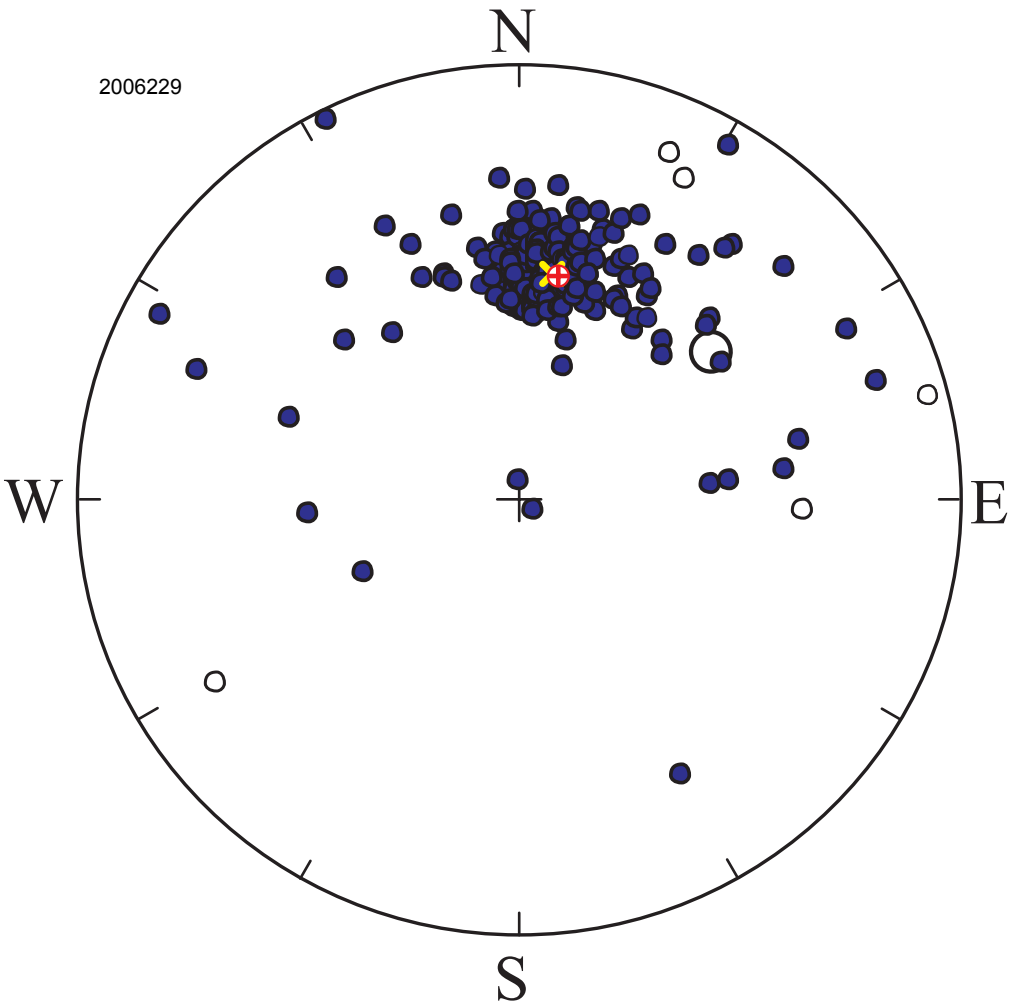

Figure DR11(Lehrmann et al.). Equal area stereographic projection showing low coercivity/low unblocking temperature magnetic ChRM direction ($D_{recent\ bbc} = 8.8^{o}$, $I_{recent\ bbc} = 45.3^{o}$, $_{95} = 6.2^{o}$, N = 267, red open circle with cross) dissimilar to the paleomagnetic direction carried by more stable magnetic minerals in the same rock ($D_{mean\ GD\ bbc} = 52.1^{o}$, $I_{mean\ GD\ bbc} = -40.4^{o}$, $_{95} = 11.9^{o}$, N = 243, large black open circle) but similar to the present day field geomagnetic field direction at Guandao ($D_{present\ day} = 9^{o}$, $I_{present\ day} = 44^{o}$, yellow cross). Stereographic shows directional data in geographic coordinates; solid circles are directions in the lower hemisphere of the projection; open circles are directions in the upper hemisphere.